View metadata, citation and similar papers at core.ac.uk

brought to you by CORE

provided by DSpace@MIT

The Astrophysical Journal Supplement Series, 181:110–128, 2009 March doi:10.1088/0067-0049/181/1/110

© 2009. The American Astronomical Society. All rights reserved. Printed in the U.S.A.

A CATALOG OF X-RAY POINT SOURCES FROM TWO MEGASECONDS OF *CHANDRA* OBSERVATIONS OF THE GALACTIC CENTER

M. P. Muno[1], F. E. Bauer[2], F. K. Baganoff[3], R. M. Bandyopadhyay[4], G. C. Bower[5], W. N. Brandt[6], P. S. Broos[6], A. Cotera[7], S. S. Eikenberry[4], G. P. Garmire[6], S. D. Hyman[8], N. E. Kassim[9], C. C. Lang[10], T. J. W. Lazio[9], C. Law[11], J. C. Mauerhan[12], M. R. Morris[12], T. Nagata[13], S. Nishiyama[14], S. Park[6], S. V. Ramírez[15], S. R. Stolovy[15], R. Wijnands[11], Q. D. Wang[16], Z. Wang[17], and F. Yusef-Zadeh[18]

[1] Space Radiation Laboratory, California Institute of Technology, Pasadena, CA 91104, USA; mmuno@srl.caltech.edu
[2] Columbia Astrophysical Laboratory, New York, NY 10027, USA; feb@astro.columbia.edu
[3] Kavli Institute for Astrophysics and Space Research, Massachusetts Institute of Technology, Cambridge, MA 02139, USA
[4] Department of Astronomy, University of Florida, Gainesville, FL 32611, USA
[5] Department of Astronomy and Radio Astronomy Laboratory, University of California, Berkeley, CA 94720-3411, USA
[6] Department of Astronomy and Astrophysics, The Pennsylvania State University, University Park, PA 16802, USA
[7] SETI Institute, 515 N. Whisman Rd., Mountain View, CA 94043, USA
[8] Department of Physics and Engineering, Sweet Briar College, Sweet Briar, VA 24595, USA
[9] Remote Sensing Division, Naval Research Laboratory, Washington, DC 20375-5351, USA
[10] Department of Physics and Astronomy, University of Iowa, Van Allen Hall, Iowa City, IA 52242, USA
[11] Astronomical Institute "Anton Pannekoek," University of Amsterdam, Kruislaan 403, 1098 SJ, The Netherlands
[12] Department of Physics and Astronomy, University of California, Los Angeles, CA 90095, USA
[13] Department of Astronomy, Kyoto University, Kyoto 606-8502, Japan
[14] National Astronomical Observatory of Japan (NAOJ), National Institutes of Natural Sciences (NINS), Tokyo 181-8588, Japan
[15] *Spitzer* Science Center, California Institute of Technology, Pasadena, CA 91125, USA
[16] Astronomy Department, University of Massachusetts, Amherst, MA 01003, USA
[17] Department of Physics, McGill University, Montreal, QC H3A 2T8, Canada
[18] Department of Physics and Astronomy, Northwestern University, Evanston, IL 60208, USA

Received 2008 May 6; accepted 2008 September 15; published 2009 March 4

ABSTRACT

We present a catalog of 9017 X-ray sources identified in *Chandra* observations of a $2^\circ \times 0.^\circ 8$ field around the Galactic center. This enlarges the number of known X-ray sources in the region by a factor of 2.5. The catalog incorporates all of the ACIS-I observations as of 2007 August, which total 2.25 Ms of exposure. At the distance to the Galactic center (8 kpc), we are sensitive to sources with luminosities of 4×10^{32} erg s^{-1} (0.5–8.0 keV; 90% confidence) over an area of 1 deg^2, and up to an order of magnitude more sensitive in the deepest exposure (1.0 Ms) around Sgr A*. The positions of 60% of our sources are accurate to $<1''$ (95% confidence), and 20% have positions accurate to $< 0.''5$. We search for variable sources, and find that 3% exhibit flux variations within an observation, and 10% exhibit variations from observation-to-observation. We also find one source, CXOUGC J174622.7−285218, with a periodic 1745 s signal (1.4% chance probability), which is probably a magnetically accreting cataclysmic variable. We compare the spatial distribution of X-ray sources to a model for the stellar distribution, and find 2.8σ evidence for excesses in the numbers of X-ray sources in the region of recent star formation encompassed by the Arches, Quintuplet, and Galactic center star clusters. These excess sources are also seen in the luminosity distribution of the X-ray sources, which is flatter near the Arches and Quintuplet than elsewhere in the field. These excess point sources, along with a similar longitudinal asymmetry in the distribution of diffuse iron emission that has been reported by other authors, probably have their origin in the young stars that are prominent at $l \approx 0.^\circ 1$.

Key words: Galaxy: center – X-rays: stars

Online-only material: machine-readable tables

1. INTRODUCTION

Stars are detectable as X-ray sources at several important stages of their lives. Pre–main-sequence (PMS) stars are X-ray sources because of their enhanced magnetic activity (Preibisch & Feigelson 2005). Massive OB and Wolf–Rayet stars produce X-rays through shocks in their stellar winds (Berghöfer et al. 1997; Gagné et al. 2005), and possibly from magnetically confined plasma close to their stellar surfaces (Waldorn & Cassinelli 2007). Neutron stars are bright X-ray sources if they are young and still have latent heat from what was once the stellar core (Walter et al. 1996), if they accelerate particles in rotating, moderate-strength ($B \sim 10^{12}$ G) fields (Gaensler & Slane 2006), or if they have extremely strong fields ($B \sim 10^{14}$ G) that decay and accelerate particles (Woods & Thompson 2006). White dwarfs, neutron stars, and black holes are bright X-ray sources if they are accreting matter from a binary companion (Warner 1995; Psaltis 2006), or in principle from the interstellar medium (see e.g., Perna et al. 2003). Therefore, X-ray surveys can be used to study the life cycles of stars, particularly their starting and ending points.

Here we present a catalog of X-ray sources detected in *Chandra* observations toward the inner $2^\circ \times 0.^\circ 8$ of the Galaxy. The region encompasses about 1% of the Galactic stellar mass (Launhardt et al. 2002), and possibly up to 10% of the Galactic population of young, massive stars (Mezger & Pauls 1979; Figer et al. 2004). Therefore, these data provide a statistically meaningful sample of the Galactic stellar population.

Previous catalogs based on *Chandra* data on the Galactic center have been published by Muno et al. (2003a) using 630

ks of data taken through 2002 June on the central $17' \times 17'$ around Sgr A*, and by Muno et al. (2006a) using observations taken through 2005 June on the inner $2^\circ \times 0.^\circ 8$ of the Galaxy. However, since the publication of these catalogs, a large amount of new data have been obtained. These data increase the number of point sources identified by a factor of 2.5. They also provide much better astrometry for individual X-ray sources. The improvement in astrometry enables the identification of rare objects such as Wolf–Rayet stars, X-ray binaries, and rotation-powered pulsars, through comparisons of our X-ray catalog with radio and infrared data sets (e.g., Mauerhan et al. 2009). Therefore, we provide here an updated catalog of point sources, which incorporates and supercedes the previous catalogs. We also describe the spatial and luminosity distributions of the X-ray sources.

Throughout this paper, we adopt a distance to the Galactic center of $D = 8$ kpc (Reid 1993; McNamara et al. 2000), and an average absorption column of $N_{\rm H} = 6 \times 10^{22}$ cm^{-2} (Baganoff et al. 2003).

2. OBSERVATIONS

As of 2007 August, the central $2^\circ \times 0.^\circ 8$ of the Milky Way has been observed with the imaging array of the *Chandra* Advanced CCD Imaging Spectrometer (ACIS-I; Weisskopf et al. 2002)[19] on numerous occasions. The majority of the new sources in this catalog come from 600 ks of exposure that we obtained in 15 40 ks pointings covering $\approx 1^\circ$ of the Galactic center. The new data since 2005 also include 370 ks on the central 20 pc around Sgr A*, 100 ks on the Arches cluster (Wang et al. 2006), and 100 ks on Sgr C. We also include sources previously identified in 630 ks of data on the inner 20 pc around Sgr A* (Muno et al. 2003a, 2004b); 30 12 ks exposures of the $2^\circ \times 0.^\circ 8$ survey obtained by Wang et al. (2002a, see also Muno et al. 2006a); and deep pointings toward the Radio Arches (50 ks; Law & Yusef-Zadeh 2004) and Sgr B2 (100 ks; Takagi et al. 2002). The dates, observation identifiers (ObsIds), durations, locations, roll angles, and some values relevant for the astrometry (Section 2.1) for each exposure are listed in Table 1. The observations in the table are sorted by right ascension and declination, so that observations near the same point are grouped.

The ACIS-I is a set of four, 1024×1024 pixel CCDs, covering a field of view (FOV) of $17' \times 17'$. When placed on-axis at the focal plane of the grazing-incidence X-ray mirrors, the imaging resolution is determined primarily by the pixel size of the CCDs, $0.''492$. The CCD frames are read out every 3.2 s, which provides the nominal time resolution of the data. The CCDs also measure the energies of incident photons within a calibrated energy band of 0.5–8 keV, with a resolution of 50–300 eV (depending on photon energy and distance from the read-out node). However in some of the earlier, shallow exposures (ObsIDs 2267 through 2296), an event filter was employed on the satellite that removed X-rays with energies below 1 keV before the data were sent to the ground. The lack of 0.5–1.0 keV photons had a minor impact on our results, because there were only 76 sources that were detected below 2 keV for which the photometry was derived entirely from the ObsIDs 2267 through 2296.[20] We omitted ObsID 242 from our analysis, because it was taken with the detector at a cooler temperature (110 K versus 120 K). A flux image and composite exposure map is displayed in Figure 1, and an adaptively smoothed three-color image is displayed in Figure 2.

The data were processed using the *Chandra* Interactive Analysis of Observations (CIAO)[21] package. The data were processed as they arrived, so we used CIAO versions 3.3 and 3.4. Information on the detectors was taken from the Calibration Database (CALDB)[22] versions 3.2.1 and 3.3.0. The differences between the two versions of the software were too minor to justify reprocessing the older portions of the data set. We only used data from ACIS-I; data from the S array was omitted because they were offset far from the aim point, and the large point-spread function (PSF) on the detector resulted in bad stellar confusion.

We started with the level 1 event files provided by the *Chandra* X-ray Center (CXC), and reprocessed the data using the tool `acis_process_events` in order to remove pixel randomization and apply more recent energy calibration. We then removed events associated with bad pixels, and applied the standard grade filters to the events and good-time filters supplied by the CXC. We applied `acis_run_hotpix` to flag events associated with cosmic rays, and removed them from the event list (we did not run `acis_detect_afterglow`, because it sometimes removes genuine X-ray events. We did, however, later remove sources that were cosmic ray afterglows; see Section 2.2). We then searched each observation for time intervals when particles encountering the detector caused the background event rate to flare to $\geqslant 3\sigma$ above the mean level, and removed them. These background flares were found in 12 observations, and lasted $< 5\%$ of the duration of each observation. Next, we applied the subpixel event-repositioning algorithm of Li et al. (2004). Finally, if an astrometric correction was available from the CXC for any observation, we applied it at this point, by modifying the header keywords for the event file, and by correcting the columns for the right ascension and declination in the aspect solution provided with the observation.

Before proceeding to explain our algorithms for source detection, we would like to explain some minor weaknesses of our approach. Unfortunately, because the data were searched for sources as they arrived, and because the exposures were highly nonuniform across the field, some parameters of our detection algorithm, particularly the detection thresholds, were not kept consistent. To compensate for this, we did two things. First, we verified the reality of each source as part of our photometric algorithm (Section 2.2). This should eliminate most spurious sources on the faint end, in a uniform manner. Second, we determined the completeness limits of our survey using Monte Carlo simulations that mimicked our source-detection algorithms (Section 2.3). This is the best way to establish what portion of our sample is complete. With the experience we have gained, in principle, we could develop a more streamlined and straightforward approach to building the initial catalog. However, it would take several months of computer time to reprocess the data, or a similar amount of time rewriting our software to be more efficient. There would be slight improvements in the final catalog, so we decided not to delay releasing our catalog any further.

We are making the data products from the following sections available in FITS format from a Web site.[23] The catalog itself will also be available with the electronic version of the paper.

[19] See also http://cxc.harvard.edu/proposer/POG/html/ACIS.html.

[20] For these sources, we underestimate the flux by $\approx 25\%$. The soft color is also systematically high. For instance, sources with $N_{\rm H} \approx 10^{21}$ cm^{-2} will have $HR0 \approx -0.5$ using a 0.5–2.0 keV soft band, and $HR0 \approx -0.3$ using a 1.0–2.0 keV soft band.

[21] http://cxc.harvard.edu/ciao/.

[22] http://cxc.harvard.edu/caldb/.

[23] http://www.srl.caltech.edu/gc_project/xray.html.

Table 1
Observations of the Central $2^\circ \times 0.^\circ 8$ of the Galaxy

Start Time	ObsID	Target	Aim Point			Astrometry			Unc.
(UT)			Exposure (ks)	R.A. (degrees, J2000)	Dec.	Roll (degrees)	N_{IR}	N_X	(arcsec)
2001 Jul 21 04:35:09	2286	GCS 28	11.6	266.01026	−29.87409	283.8	···	···	0.5
2001 Jul 21 08:03:39	2289	GCS 29	11.6	265.81895	−29.77175	283.8	···	···	0.5
2001 Jul 21 11:32:10	2290	GCS 30	11.6	265.62792	−29.66920	283.8	···	···	0.5
2000 Aug 30 16:59:32	658	1E 1740.7-2942	9.2	265.97607	−29.75041	270.8	···	···	0.5
2001 Jul 20 18:09:40	2278	GCS 25	11.6	266.12796	−29.70796	283.8	···	···	0.5
2006 Jun 27 16:38:52	7042	Deep GCS 12	14.4	265.92331	−29.62836	297.2	8	···	0.2
2006 Jul 1 13:53:08	7346	Deep GCS 12	15.2	265.92332	−29.62846	297.2	···	8	0.3
2006 Jun 28 16:24:41	7345	Deep GCS 12	10.0	265.92328	−29.62841	297.2	···	2	0.4
2001 Jul 20 21:38:10	2281	GCS 26	11.6	265.93676	−29.60580	283.8	···	8	0.2
2007 Apr 29 06:03:16	7043	Deep GCS 13	34.2	265.72756	−29.51198	82.9	9	···	0.13
2001 Jul 21 01:06:39	2283	GCS 27	11.6	265.74591	−29.50336	283.8	···	7	0.2
2001 Jul 20 08:00:49	2270	GCS 22	10.6	266.24516	−29.54168	283.8	···	···	0.5
2005 Jul 22 01:58:12	5892	Sgr C	97.9	266.08819	−29.43665	278.0	25	···	0.08
2001 Jul 20 11:12:40	2272	GCS 23	11.6	266.05414	−29.43966	283.8	···	15	0.2
2006 Sep 15 14:54:55	7041	Deep GCS 10	19.9	265.84657	−29.35563	269.0	4	···	0.2
2006 Sep 27 01:21:42	8214	Deep GCS 10	17.7	265.84656	−29.35560	269.0	4	···	0.2
2001 Jul 20 14:41:10	2275	GCS 24	11.6	265.86352	−29.33749	283.8	···	4	0.2
2007 Apr 25 14:04:05	7040	Deep GCS 8	36.7	266.35283	−29.38207	84.0	15	···	0.10
2001 Jul 19 06:41:38	2296	GCS 19	11.1	266.36200	−29.37542	283.8	···	6	0.2
2006 Oct 31 03:58:52	7038	Deep GCS 6	19.7	266.15861	−29.29070	268.2	3	···	0.2
2007 Feb 19 01:49:07	8459	Deep GCS 6	19.3	266.15788	−29.27900	91.6	···	16	0.3
2001 Jul 19 10:01:48	2267	GCS 20	8.7	266.17124	−29.27356	283.8	···	11	0.2
2006 Jul 27 05:11:38	7039	Deep GCS 7	37.8	265.96598	−29.18723	276.1	7	···	0.17
2001 Jul 20 04:37:11	2268	GCS 21	10.8	265.98088	−29.17148	283.8	···	7	0.2
2006 Aug 24 20:26:37	7037	Deep GCS 5	39.4	266.47130	−29.22528	275.2	12	···	0.12
2001 Jul 18 20:49:28	2291	GCS 16	10.6	266.47846	−29.20889	283.8	···	11	0.2
2006 Jul 26 18:06:34	7035	Deep GCS 3	38.0	266.27807	−29.12211	276.3	5	···	0.12
2001 Jul 19 00:01:18	2293	GCS 17	11.1	266.28790	−29.10730	283.8	···	21	0.2
2007 Jul 19 20:45:11	8567	Deep GCS 4	19.5	266.09028	−29.02150	278.3	10	···	0.18
2007 Jul 9 16:12:13	7036	Deep GCS 4	19.9	266.09096	−29.02114	283.5	7	···	0.15
2001 Jul 19 03:21:28	2295	GCS 18	11.1	266.09774	−29.00538	283.8	···	8	0.2
2001 Jul 14 01:51:10	1561b	Sgr A*	13.5	266.41344	−29.01281	264.7	···	24	0.12
2000 Oct 26 18:15:11	1561a	Sgr A*	35.7	266.41344	−29.01281	264.7	···	68	0.06
2007 Jul 20 02:27:01	7557	Sgr A*	5.0	266.42069	−29.01498	278.4	···	9	0.15
2004 Aug 28 12:03:59	5360	Sgr A*	5.1	266.41477	−29.01211	271.0	···	9	0.1
2005 Jul 29 19:51:11	5952	Sgr A*	43.1	266.41508	−29.01219	275.5	···	76	0.06
2005 Jul 30 19:38:31	5953	Sgr A*	45.4	266.41506	−29.01218	275.3	···	78	0.06
2005 Jul 24 19:58:27	5950	Sgr A*	48.5	266.41519	−29.01222	276.7	···	64	0.06
2005 Jul 27 19:08:16	5951	Sgr A*	44.6	266.41512	−29.01219	276.0	···	66	0.06
2006 Jul 17 03:58:28	6363	Sgr A*	29.8	266.41541	−29.01228	279.5	···	59	0.06
2006 Jul 30 14:30:26	6643	Sgr A*	5.0	266.41510	−29.01218	275.4	···	11	0.18
2005 Aug 1 19:54:13	5954	Sgr A*	18.1	266.41502	−29.01215	274.9	···	36	0.1
2006 Sep 25 13:50:35	6645	Sgr A*	5.1	266.41448	−29.01195	268.3	···	7	0.18
2006 Aug 22 05:54:34	6644	Sgr A*	5.0	266.41484	−29.01202	271.7	···	10	0.18
2004 Jul 6 22:29:57	4684	Sgr A*	49.5	266.41597	−29.01236	285.4	···	94	0.06
2004 Jul 5 22:33:11	4683	Sgr A*	49.5	266.41605	−29.01238	286.2	···	98	0.06
2006 Oct 29 03:28:20	6646	Sgr A*	5.1	266.41425	−29.01178	264.4	···	9	0.18
2006 Jul 4 11:01:35	6642	Sgr A*	5.1	266.41633	−29.01237	288.4	···	7	0.18
2003 Jun 19 18:28:55	3549	Sgr A*	24.8	266.42092	−29.01052	346.8	···	49	0.06
2006 Jun 1 16:07:52	6641	Sgr A*	5.1	266.42018	−29.00440	69.7	···	7	0.18
2002 May 22 22:59:15	2943	Sgr A*	34.7	266.41991	−29.00407	75.5	···	86	0.15
2002 Jun 3 01:24:37	3665	Sgr A*	89.9	266.41992	−29.00407	75.5	···	162	0.06
2002 May 25 15:16:03	3392	Sgr A*	165.8	266.41992	−29.00408	75.5	23	···	0.06
2002 May 28 05:34:44	3393	Sgr A*	157.1	266.41992	−29.00407	75.5	···	759	0.06
2002 May 24 11:50:13	3663	Sgr A*	38.0	266.41993	−29.00407	75.5	···	82	0.10
2006 Apr 11 05:33:20	6639	Sgr A*	4.5	266.41890	−29.00369	86.2	···	11	0.18
2006 May 3 22:26:26	6640	Sgr A*	5.1	266.41935	−29.00383	82.8	···	8	0.18
2005 Feb 27 06:26:04	6113	Sgr A*	4.9	266.41870	−29.00353	90.6	···	6	0.12
2002 May 7 09:25:07	2954	Sgr A*	12.5	266.41938	−29.00374	82.1	···	25	0.15
2007 Feb 11 06:16:55	7554	Sgr A*	5.1	266.41853	−29.00343	92.6	···	11	0.2
2002 Feb 19 14:27:32	2951	Sgr A*	12.4	266.41867	−29.00335	91.5	···	35	0.15
2002 Mar 23 12:25:04	2952	Sgr A*	11.9	266.41897	−29.00343	88.2	···	23	0.15

Table 1
(Continued)

Start Time	ObsID	Target	Aim Point			Astrometry			Unc.
(UT)			Exposure (ks)	R.A. (degrees, J2000)	Dec.	Roll (degrees)	N_{IR}	N_X	(arcsec)
2002 Apr 19 10:39:01	2953	Sgr A*	11.7	266.41923	−29.00349	85.2	···	28	0.15
2007 Mar 25 22:56:07	7555	Sgr A*	5.1	266.41420	−29.00013	88.0	···	10	0.15
2001 Jul 18 11:13:58	2282	GCS 13	10.6	266.59457	−29.04224	283.8	···	···	0.5
2001 Jul 18 14:25:48	2284	GCS 14	10.6	266.40415	−28.94090	283.8	···	23	0.2
2007 Feb 22 03:29:33	7034	Deep GCS 1	39.6	266.20175	−28.83783	91.0	36	···	0.03
2001 Jul 18 17:37:38	2287	GCS 15	10.6	266.21412	−28.83905	283.8	···	18	0.2
2000 Jul 7 19:05:19	945	GC Arc	48.8	266.58221	−28.87193	284.4	12	···	0.12
2004 Jun 9 08:50:32	4500	Arches cluster	98.6	266.48260	−28.81691	55.2	26	···	0.10
2007 Feb 14 03:59:44	7048	Deep GCS 27	38.2	266.71020	−28.87828	92.3	6	···	0.17
2001 Jul 18 00:48:28	2273	GCS 10	11.2	266.71024	−28.87570	283.8	···	6	0.2
2001 Jul 18 04:16:58	2276	GCS 11	11.6	266.52002	−28.77435	283.8	···	12	0.2
2001 Jul 18 07:45:28	2279	GCS 12	11.6	266.33030	−28.67280	283.8	···	9	0.2
2007 Feb 24 04:56:00	7047	Deep GCS 26	36.7	266.31970	−28.66905	90.8	9	···	0.17
2007 Jul 19 10:04:05	7046	Deep GCS 25	36.5	266.82943	−28.72059	278.4	18	···	0.10
2001 Jul 17 14:11:51	2288	GCS 7	11.1	266.82550	−28.70883	283.8	···	10	0.2
2006 Nov 1 14:11:44	7044	Deep GCS 23	37.9	266.63030	−28.61480	268.2	12	···	0.11
2001 Jul 17 17:51:28	2292	GCS 8	11.6	266.63554	−28.60780	283.8	···	12	0.2
2001 Jul 17 21:19:58	2294	GCS 9	11.6	266.44598	−28.50635	283.8	···	8	0.2
2007 Feb 23 07:15:57	7045	Deep GCS 24	37.0	266.43720	−28.50006	90.9	9	···	0.13
2001 Jul 16 11:52:55	2277	GCS 4	10.4	266.94060	−28.54206	283.8	···	···	0.5
2000 Mar 29 09:44:36	944	Sgr B2	97.5	266.78070	−28.44160	87.8	23	···	0.10
2001 Jul 16 15:01:25	2280	GCS 5	10.4	266.75080	−28.44106	283.8	···	9	0.2
2001 Jul 16 18:09:55	2285	GCS 6	10.4	266.56137	−28.33985	283.4	···	···	0.5
2001 Jul 16 02:15:50	2269	GCS 1	10.5	267.05519	−28.37520	283.8	···	···	0.5
2001 Jul 16 05:35:55	2271	GCS 2	10.4	266.86561	−28.27427	283.8	···	···	0.5
2001 Jul 16 08:44:25	2274	GCS 3	10.4	266.67640	−28.17316	283.8	···	···	0.5

Notes. The columns are: the date and time of the observation (UT), the observation identifier, the target name, the exposure time (ks), the right ascension and declination (J2000), the roll angle of the satellite, the number of 2MASS sources that we used to align the astrometry for the deepest observations at any point, the number of X-ray matches that we used to align the astrometry of the shallower observations to the deepest ones, and the 1σ uncertainties on the astrometry as determined from the standard deviations in the means of the offsets between the input and trial catalogs. The observations have been sorted first by declination, then by right ascension, so that observations of the same region are grouped in the table.

2.1. Source Detection and Initial Localization

Source detection and localization were approached iteratively. We first searched for point sources in each observation separately. The locations of the point sources found in the first stage were used to refine the astrometry. Second, the astrometrically corrected images were combined to search for fainter point sources. Finally, the source lists from the individual observations were merged with those from the combined images.

We searched each observation individually for point sources using the wavelet decomposition algorithm `wavdetect` (Freeman et al. 2002). We employed the default "Mexican Hat" wavelet, and used a sensitivity threshold of 10^{-7}. This threshold roughly corresponds to the chance of detecting a spurious source in an area corresponding to the PSF, if the local background is spatially uniform. For the earlier data, taken before 2006, we used images at three different resolutions: one at $0\farcs5$ resolution covering the inner 1024×1024 pixels, one at $1''$ resolution covering the inner 2048×2048 pixels, and one at $2''$ resolution covering the entire field. For later observations, we simplified the process and used only two resolutions: $0\farcs5$ covering the inner 2048×2048 pixels, and $2''$ covering the entire field. Using a test field, we confirmed that there was no difference in the number of sources detected using the two techniques; the only difference is that the technique that used three, smaller images was computationally faster. We used wavelet scales that increased by a factor of $\sqrt{2}$, over the range of 1–4 pixels for the $0\farcs5$ image, 1–8 pixels for the $1''$ image, and 1–16 pixels for the $2''$ image. For each resolution, we made images in three energy bands: 0.5–8.0 keV to cover the full bandpass, 0.5–2.0 keV to provide sensitivity to foreground sources, and 4–8 keV to provide sensitivity to highly absorbed sources. For each image, a matching exposure map was generated for photons with an energy of 4 keV, so that the wavelet algorithm could keep track of regions with rapidly varying exposure, such as bad columns and the edges of the CCDs.

The lists derived from each image resolution were combined to form master source lists for each energy band. We found that the positions would be most accurate from the sources identified in the image with the finest resolution. Therefore, we discarded sources from the lower resolution images if their separations from sources identified at high resolution were smaller than the radii of the 90% contour of the PSF. In this way, we produced three lists for each observation, one for each energy band.

Next, we used the point sources detected so far to register the absolute astrometry to the Two Micron All Sky Survey (2MASS; Skrutskie et al. 2006). The 2MASS frame is consistent with the International Celestrial Reference System to within 15 mas. We compared the positions of 2MASS sources to those of X-ray sources detected in the 0.5–2.0 keV band that were identified by `wavdetect` as having $> 3\sigma$ significance, and identified matches as those with offsets $< 1''$. The offsets between the 2MASS and *Chandra* frames were computed using a least-chi-squared

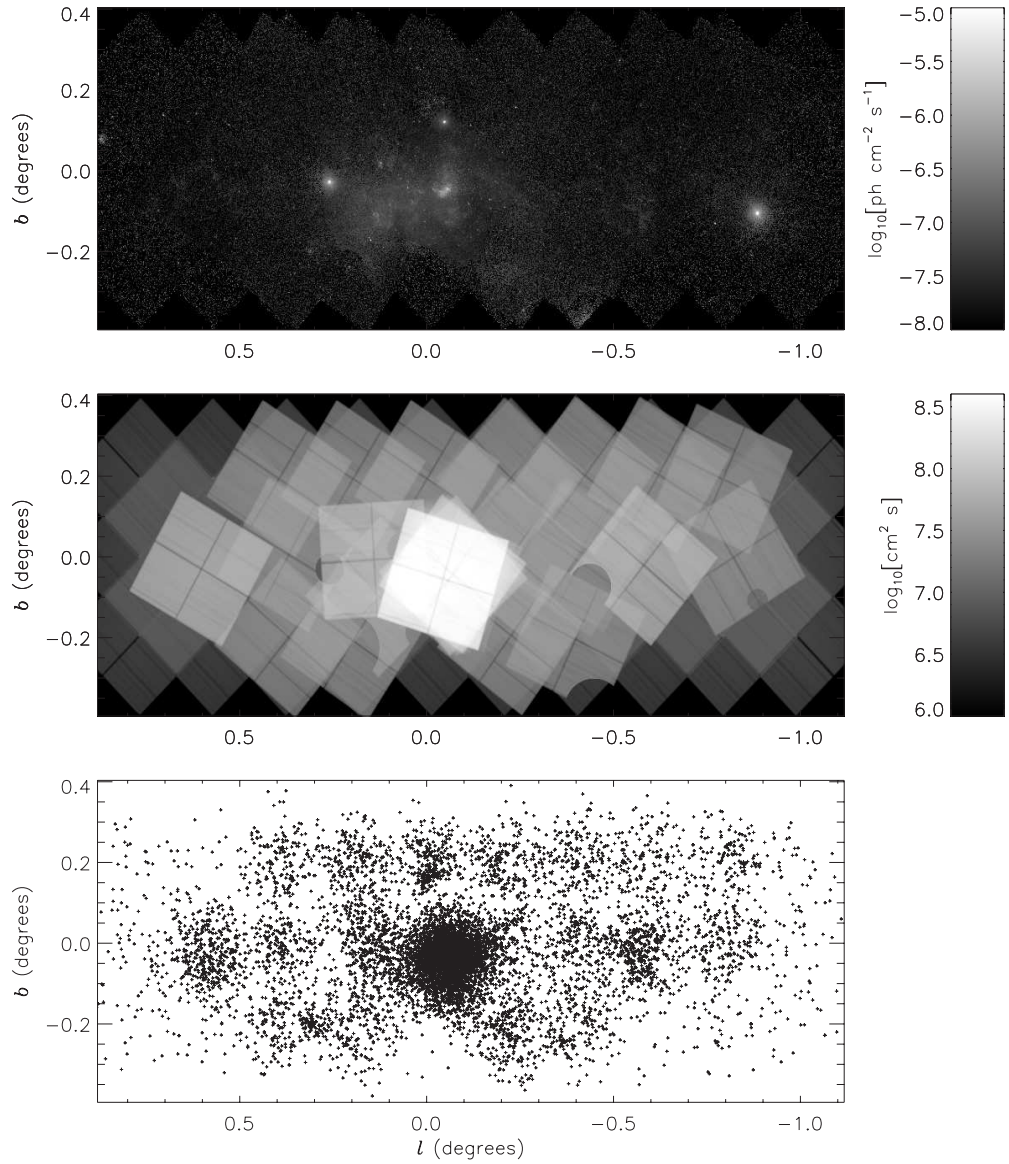

Figure 1. Basic results from the survey. The top panel contains a composite image of the field, in which the counts have been divided by an exposure map to provide an estimate of the 0.5–8.0 keV flux. The middle panel contains the exposure map for an energy of 4 keV, in units of the product of the effective area times the exposure time. Some holes are visible where we have excluded regions where bright transients and their associated dust-scattering halos were present in some individual observations, because these degraded the sensitivity. The bottom panel illustrates the locations of point sources in our sample. The regions with the largest exposure have the greatest concentrations of point sources.

algorithm. The X-ray sources that we used for astrometry are flagged in Table 2 (see Section 2.6).

For observations longer than 20 ks, we found between 3 and 36 X-ray sources in the soft band that could be associated unambiguously with stars in the 2MASS catalog, and so we used the average offsets between the X-ray and the infrared sources to correct the astrometry of the X-ray observations. We evaluated the accuracy of the registration based on the standard deviation in the mean of the offsets of the individual stars. The registration was accurate to 0.″06 for the deepest exposures, and to 0.″2 for the shallower ones (1σ). Unfortunately, for exposures shorter than 20 ks, too few X-ray sources were found with 2MASS counterparts to correct the astrometry to better than the default value, 0.″5 (1σ).

Once the deepest observation at each point was registered to the 2MASS frame, the shallower observations were registered using the offsets of X-ray sources detected in the 0.5–8.0 keV band in pairs of observations. Between 2 and 759 X-ray sources matched between the deepest and the shallower observations, depending upon the exposure time of the shallower observation. The uncertainty in the astrometry of each observation is listed in the last column of Table 1. The composite image and exposure map for our survey are displayed in Figure 1.

Having corrected the astrometry for fields that included deep observations, we then combined subsets of the images in order to perform a deeper search for point sources. Two wavelet algorithms were used, on the series of images listed below. First, the tool `wavdetect` (Freeman et al. 2002) was used to identify point sources in the following.

1. Composite images made from all of the observations of Sgr A*. Twelve 1024 × 1024 images were made, in four resolutions (0.″25, 0.″5, 1″, and 2″) and using three energy bands for each resolution (0.5–8.0 keV, 0.5–2.0 keV, and 4–8 keV).
2. Three sets of composite images made from observations of Sgr A* in 2002, 2004, and 2005. These images were

Table 2
Galactic Center X-Ray Source Locations and Extraction Information

Number	Name (CXOUGC J)	R.A. (degrees, J2000)	Dec.	σ_X (arcsec)	Pos.	Field	Band	Offset (arcmin)	N_{Obs}	Exposure (s)	f_{PSF}	E_{PSF} (keV)	R_{src} (arcsec)	F_{sens} (10^{-7} cm^{-2} s^{-1})	Flags
1	2	3	4	5	6	7	8	9	10	11	12	13	14	15	16
1	174457.1−285740	266.23813	−28.96121	1.8	c	Full	Soft	9.8	14	372669	0.90	1.50	9.8	32.2	s
2	174457.4−285622	266.23941	−28.93967	2.0	c	2004	Full	10.2	15	377775	0.90	4.51	11.2	26.8	lb
3	174459.1−290604	266.24620	−29.10122	1.3	c	Full	Full	10.8	12	571227	0.87	4.51	11.8	9.0	sc
4	174459.9−290324	266.24982	−29.05683	2.0	c	2002	Full	9.3	23	923358	0.90	4.51	9.6	10.0	g
5	174459.9−290538	266.24994	−29.09415	1.5	c	Full	Hard	10.3	18	732385	0.90	4.51	11.5	9.6	b
6	174500.2−290057	266.25113	−29.01598	2.6	w	2005	Soft	8.6	18	423683	0.76	1.50	6.3	22.7	c
7	174500.6−290443	266.25244	−29.07895	1.3	c	Full	Full	9.7	20	810677	0.69	4.51	6.8	10.2	lc
8	174501.3−285501	266.25580	−28.91719	0.5	w	242	Full	10.1	18	423686	0.77	4.51	7.9	23.3	lcp
9	174501.4−290408	266.25598	−29.06908	1.1	c	Full	Hard	9.3	26	945772	0.80	4.51	7.6	10.2	c
10	174501.7−290313	266.25732	−29.05367	1.1	c	Full	Hard	8.9	27	956403	0.90	4.51	9.3	11.5	gb
11	174501.8−290206	266.25760	−29.03520	1.1	c	Full	Full	8.6	26	943948	0.69	4.51	5.3	10.8	c
12	174501.9−285719	266.25827	−28.95553	1.8	c	Full	Soft	8.9	18	423686	0.69	1.50	5.1	24.7	lbc
13	174502.2−285749	266.25946	−28.96381	1.0	c	5951	Full	8.7	18	423686	0.87	4.51	7.5	23.5	c
14	174502.4−290205	266.26007	−29.03492	1.1	c	2002	Soft	8.5	27	956403	0.70	1.50	4.9	9.7	c
15	174502.4−290453	266.26039	−29.08160	1.4	c	Full	Soft	9.4	29	967611	0.88	1.50	8.4	11.4	···
16	174502.5−290415	266.26077	−29.07086	2.0	w	Full	Tile	9.1	29	967611	0.75	4.51	6.5	11.2	lbc
17	174502.7−290127	266.26101	−29.02376	1.6	c	3392	Full	8.3	27	956431	0.89	4.51	7.7	9.2	···
18	174502.8−290429	266.26198	−29.07480	1.3	c	Full	Soft	9.1	30	972102	0.77	1.50	6.1	11.1	bc
19	174502.9−285920	266.26222	−28.98968	1.1	c	Full	Full	8.2	18	423686	0.90	4.51	7.3	19.4	···
20	174503.7−285805	266.26531	−28.96845	1.2	c	2005	Full	8.3	20	440908	0.70	4.51	4.8	21.7	bc
21	174503.8−290004	266.26584	−29.00112	0.9	c	Full	Full	8.0	30	985035	0.70	4.51	4.5	9.5	gc
22	174504.1−285902	266.26740	−28.98400	4.7	w	6646	Soft	8.0	30	955147	0.74	1.50	4.7	13.8	bc
23	174504.2−285653	266.26758	−28.94817	1.4	c	242	Full	8.6	22	457849	0.90	4.51	7.8	22.7	l
24	174504.2−290410	266.26764	−29.06977	1.5	c	2002	Soft	8.7	34	1011810	0.70	1.50	4.9	8.7	c
25	174504.2−290610	266.26841	−29.10258	1.9	c	2005	Hard	9.8	32	988816	0.83	4.51	8.5	10.3	c

Note. A portion of the full table is shown here, for guidance as to its form and content. The columns are described in the text.

(This table is available in its entirety in a machine-readable form in the online journal. A portion is shown here for guidance regarding its form and content.)

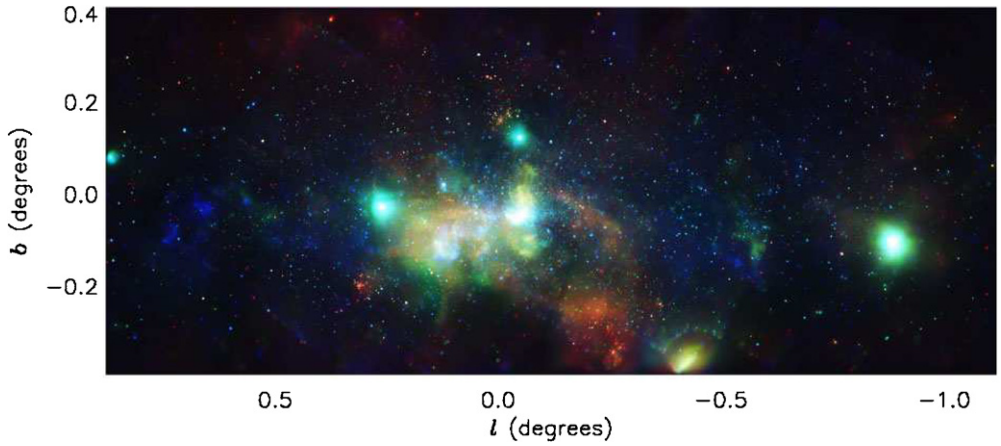

Figure 2. Three-color image of the survey area. Red is 1–3 keV, green is 3–5 keV, and blue is 5–8 keV. Each band was adaptively smoothed using the CIAO tool `csmooth`, and then normalized using an exposure map. Some artifacts can be seen at the boundaries of chip edges, particularly near where bright, transient X-ray sources appeared.

designed to be sensitive to faint, variable sources. The same image resolutions and energy bands were used as for the composite image of all of the Sgr A* data.

3. Composite images made from three pointings that were taken with same roll angle, because the original 40 ks exposure had to be split up to accommodate scheduling constraints (ObsIDs 7038, 7041, and 7042). Three images were made for each aim point, one for each of the 0.5–8.0 keV, 0.5–2.0 keV, and 4–8 keV energy bands. Each image was made at 0.″5 resolution, and had 2048 × 2048 pixels.

The parameters used with `wavdetect` were the same as for the individual observations.

Second, we used the tools `wvdecomp` and `findpeak` in the *zhtools* package written by A. Vikhlinin[24] to search for faint sources that fell below the `wavdetect` threshold. We searched on wavelet scales of 1–3 pixels, and required that a candidate source be identified with a minimum signal-to-noise of 4.5, corresponding to 16 spurious sources per 2048 × 2048 pixel image. Five iterations of the search procedure were performed. The tool `wvdecomp` iteratively cleans the image of point sources identified in previous passes through the data, so it is more efficient at separating close pairs of sources. Moreover, unlike `wavdetect`, `wvdecomp` does not use any information about the

[24] http://hea-www.harvard.edu/RD/zhtools.

shape of the PSF in searching for sources, so it is better at identifying point sources when observations with very different aim points have been combined. Therefore, we used `wvdecomp` on composite images generated from all data covering the positions at which deep observations were obtained (i.e., ObsIDs 3392, 4500, 5892, 7034–7048, and 944). Each image was produced with 2048 × 2048 pixels at 0.″5 resolution for the 0.5–8.0 keV band.

We then generated a list containing the unique sources, by merging the lists generated by `wavdetect` from individual observations and from combined images, and from the lists generated by `wvdecomp`. We found that almost all the duplicates could be removed by identifying sources with separations smaller than the prescription for positional uncertainties in Brandt et al. (2001): for sources offset from the center of each image by $\theta < 5'$, the separation was cut at 0.″6, whereas for larger offsets it was cut at $0.''6 + (\theta - 5.0)/8.75$ (θ is in arcminutes).[25] For each image, we gave preference to positions from the full-band sources, then from the soft sources, and finally from the hard sources. Across observations, the priority was given to the deeper observations, and to the sources detected with `wavdetect` over those detected with `wvdecomp`. We examined the final list visually by comparing it to images of the survey fields, and we removed several hundred sources that were portions of extended, diffuse features (from Muno et al. 2007), and a couple dozen duplicates that were not identified automatically. Finally, two sources were not picked up by the detection algorithms because they were blended with nearby, brighter sources. We added these to our catalog by hand (CXOUGC J174502.8−282505 and J174617.4−281246).

At this stage, we considered our source lists to be provisional, both because the search algorithms used nonuniform parameters, and because the large, spatially variable background was likely to cause our wavelet algorithms to generate a significant number of spurious sources. In order to confirm their validity, we next computed photometry for each provisional source.

2.2. Photometry

We computed aperture photometry for each source using the ACIS Extract package, versions 3.96, 3.101, and 3.128 (Broos et al. 2002; Townsley et al. 2003; Getman et al. 2005), along with some custom code. The algorithm proceeded in several steps.

First, for each source and each observation, we obtained a model PSF with the CIAO tool `mkpsf`. For most sources, we used a PSF for a fiducial energy of 4.5 keV. However, if a source was only detected with `wavdetect` in the soft band, we used a PSF for an energy of 1.5 keV. To determine a region from which we would extract source counts, we then constructed a polygon enclosing 90% of the PSF. If the polygons for two sources overlapped in the observations in which the sources were closest to the aim point, we generated a smaller polygon. The final extraction regions were enclosed between 70% and 90% of the PSF. Sources for which the PSF fraction was < 90% were considered to be confused. Moreover, because the PSF grows rapidly beyond 7′ from the aim point, we also considered sources to be confused if they were located beyond 7′ from the aim point and their PSFs overlapped. Photometry was not computed for observations in which confused sources fell > 7′ off-axis. Fortunately, these second type of confused sources were always located on-axis in another observation, or else they would not have been identified. Finally, for similar reasons, we only computed photometry for sources that lay within 7′ of Sgr A* if the relevant observations had Sgr A* as the aim point.

Second, we extracted source event lists, source spectra, effective area functions, and response matrices for each source in each observation. The detector responses and effective areas were obtained using the CIAO tools `mkacisrmf` and `mkarf`, respectively. For each source, the spectra from all of the relevant observations were summed. The responses and effective areas were averaged, weighted by the exposures in each observation.

Third, we extracted background events from circular regions surrounding each point source in each observation, omitting events that fell within circles that circumscribed ≈ 90% of the PSFs around any point sources. The background regions were chosen to contain ≈ 100 total counts for the wide survey, and ≈ 1000 total counts for the deeper Sgr A* field. Fewer than 1% of the counts in the background region originate from known point sources. For each source, the background spectra from all of the relevant observations were scaled by the integrals of the exposure maps (in units of cm^2 s) over the source and the background regions, and then summed to create composite background spectra.

Fourth, we eliminated spurious sources. We compared the number of source and background counts to estimate the probability that no source was present, based on Poisson statistics (Weisskopf et al. 2007). If a source had a > 10% chance of being spurious, we eliminated it from our catalog. We eliminated 1962 sources in this way. We also eliminated sources in which the majority of events were cosmic ray afterglows. Specifically, we removed 46 sources because the events associated with the candidate source fell in a single pixel during 5–10 consecutive frames. Our final catalog contains 9017 X-ray sources, and is listed in Table 2. The majority of sources, 7152, were found with `wavdetect`. Of the sources detected with `wavdetect`, 4823 were detected in the full band, 948 in the soft band, and 1381 in the hard band. Another 1865 sources were only detected with `wvdecomp`. In the Sgr A* field alone, we found 3441 sources with `wavdetect`, of which 2715 were detected in the full composite image, 275 in 2002, 48 in 2004, 90 in 2005, and 313 in individual observations. An additional 364 were found in the Sgr A* field with `wvdecomp`.

Fifth, we compared the source and the background spectra using the Kolmogorov–Smirnov (KS) statistic, in order to flag potentially spurious objects that could be variations in the background. Caution should be used when studying sources that resemble the background. For instance, in the central parsec around Sgr A*, there is an overabundance of faint ($\lesssim 10^{-6}$ photons cm^{-2} s^{-1}), soft point sources that have spectra consistent with that of the background warm plasma (note that almost all of the excess bright sources that we discuss in Section 3.1 do have spectra that are distinct from the background). Therefore, we suspect that most of these are ∼ 0.1 pc scale variations in the density of that plasma. Unfortunately, we cannot be certain. Indeed, the spectrum of the bright X-ray source associated with IRS 13 (CXOUGC J174539.7−290029) resembles the background according to the KS test. If the diffuse background is merely unresolved point sources (Wang et al. 2002a; Revnivtsev et al. 2006; Revnivtsev & Sazonov 2007), then most faint point sources should have spectra that resemble the background.

[25] We use a different prescription in Section 2.4 for the uncertainties on the positions in the catalog.

Table 3
Galactic Center X-Ray Source Photometry

No.	Name CXOUGC J	$\log(P_{KS})$	$C_{t,0.5-2}$	$C_{b,0.5-2}$	$C_{net,0.5-2}$	$C_{t,2-8}$	$C_{b,2-8}$	$C_{net,2-8}$	$F_{0.5-2}$ (10^{-7} cm^{-2} s^{-1})	F_{2-8}	$\bar{E}$	HR_0	HR_1	HR_2
1	2	3	4	5	6	7	8	9	10	11	12	13	14	15
1	174457.1−285740	−4.50	86	26.3	$59.7^{+16.4}_{-14.0}$	185	186.4	< 23.7	6.8	···	1.0	< -0.555	···	···
2	174457.4−285622	−0.09	52	53.0	< 14.2	357	298.8	$58.2^{+33.6}_{-28.3}$	···	8.2	4.6	···	> 0.031	$-0.169^{+0.612}_{-0.615}$
3	174459.1−290604	−2.57	118	88.1	$29.9^{+18.8}_{-16.7}$	498	349.1	$148.9^{+32.3}_{-40.4}$	1.9	13.3	3.5	$0.116^{+0.415}_{-0.411}$	$0.299^{+0.294}_{-0.263}$	$-0.254^{+0.254}_{-0.396}$
4	174459.9−290324	−1.09	96	91.1	< 15.0	369	334.6	$34.4^{+29.6}_{-28.9}$	···	2.4	3.1	> -0.066	< 0.194	···
5	174459.9−290538	−0.97	107	115.0	< 22.7	550	434.9	$115.1^{+40.2}_{-40.2}$	···	10.3	4.8	···	> 0.243	$-0.012^{+0.357}_{-0.374}$
6	174500.2−290057	−1.99	41	25.1	$15.9^{+11.4}_{-9.5}$	138	133.5	< 19.2	1.5	···	0.5	$-0.065^{+0.506}_{-0.779}$	< 0.006	···
7	174500.6−290443	−1.90	50	44.5	< 10.8	316	200.3	$115.7^{+31.5}_{-27.0}$	···	11.1	4.6	···	> 0.400	$0.053^{+0.247}_{-0.246}$
8	174501.3−285501	−40.35	175	69.8	$105.2^{+22.4}_{-21.0}$	13585	3163.7	$10421.3^{+165.9}_{-165.9}$	9.7	1625.1	4.7	$0.861^{+0.027}_{-0.028}$	$0.462^{+0.021}_{-0.021}$	$0.146^{+0.017}_{-0.017}$
9	174501.4−290408	−4.12	92	100.1	< 21.7	523	371.2	$151.8^{+38.3}_{-38.3}$	···	11.9	5.4	···	> 0.029	$0.578^{+0.242}_{-0.230}$
10	174501.7−290313	−0.76	89	104.1	< 25.7	561	433.0	$128.0^{+40.4}_{-40.4}$	···	8.7	5.1	> 0.390	$0.163^{+0.596}_{-0.547}$	$0.351^{+0.362}_{-0.335}$
11	174501.8−290206	−2.37	39	34.2	< 10.1	248	144.9	$103.1^{+27.7}_{-24.1}$	···	8.0	4.6	···	> 0.440	$-0.058^{+0.244}_{-0.253}$
12	174501.9−285719	−0.88	41	19.9	$21.1^{+11.2}_{-9.7}$	163	143.6	$19.4^{+18.6}_{-18.1}$	2.1	3.2	3.2	< -0.296	> -0.014	< 0.288
13	174502.2−285749	−5.62	60	38.7	$21.3^{+13.3}_{-12.0}$	378	281.3	$96.7^{+36.2}_{-27.7}$	1.6	6.6	2.6	$0.517^{+0.257}_{-0.238}$	$-0.221^{+0.259}_{-0.259}$	< -0.564
14	174502.4−290205	−2.76	70	31.1	$38.9^{+12.5}_{-14.5}$	159	109.7	$49.3^{+19.1}_{-21.9}$	1.8	3.2	2.8	$-0.570^{+0.288}_{-0.417}$	$0.417^{+0.568}_{-0.391}$	$-0.339^{+0.409}_{-0.640}$
15	174502.4−290453	−7.28	172	91.6	$80.4^{+24.0}_{-19.0}$	349	340.4	< 27.8	3.3	···	0.9	$-0.577^{+0.233}_{-0.333}$	< -0.064	···
16	174502.5−290415	−0.04	69	56.4	$12.6^{+10.5}_{-12.5}$	218	194.8	< 15.4	0.6	···	3.1	$0.071^{+0.948}_{-0.918}$	< -0.149	···
17	174502.7−290127	−1.10	80	101.9	< 30.8	372	312.8	$59.2^{+34.1}_{-28.8}$	···	3.4	6.3	···	> -0.097	$0.161^{+0.550}_{-0.683}$
18	174502.8−290429	−0.49	139	86.3	$52.7^{+18.3}_{-20.0}$	308	279.6	< 18.9	2.2	···	2.9	< -0.609	···	> 0.065
19	174502.9−285920	−1.28	43	33.7	< 7.5	234	164.0	$70.0^{+27.0}_{-23.2}$	···	9.0	4.9	···	> 0.581	$0.084^{+0.323}_{-0.294}$
20	174503.7−285805	−0.63	17	15.3	< 6.9	143	75.0	$68.0^{+19.4}_{-19.6}$	···	11.2	4.7	> 0.181	$0.210^{+0.596}_{-0.445}$	$0.320^{+0.312}_{-0.294}$
21	174503.8−290004	−1.94	56	51.9	< 12.8	341	232.2	$108.8^{+30.3}_{-30.2}$	···	6.8	4.3	> 0.108	$0.418^{+0.436}_{-0.293}$	$-0.165^{+0.292}_{-0.322}$
22	174504.1−285902	−0.22	27	19.9	< 6.9	90	71.8	$18.2^{+15.4}_{-14.1}$	···	1.2	2.7	> -0.282	$0.228^{+0.767}_{-0.716}$	< -0.148
23	174504.2−285653	−2.59	46	56.2	< 18.2	419	353.4	$65.6^{+34.7}_{-32.1}$	···	10.3	6.5	···	···	> 0.435
24	174504.2−290410	−2.66	121	66.9	$54.1^{+16.6}_{-19.1}$	250	249.8	< 27.0	2.1	···	0.9	< -0.518	···	···
25	174504.2−290610	−1.31	129	124.1	< 19.0	543	496.0	$47.0^{+41.3}_{-41.3}$	···	3.1	4.6	···	> 0.406	$-0.140^{+0.485}_{-0.851}$

Note. A portion of the full table is shown here, for guidance as to its form and content. The columns are described in the text.

(This table is available in its entirety in a machine-readable form in the online journal. A portion is shown here for guidance regarding its form and content.)

Sixth, we computed the net counts in the 0.5–2.0 keV, 2.0–8.0 keV, 2.0–3.3 keV, 3.3–4.7 keV, and 4.7–8.0 keV bands. We estimated the photon flux from each source, by dividing the net counts by the average of the effective area function in each band. Table 3 lists the 0.5–2.0 keV and 2–8 keV fluxes, the latter of which is the sum of the fluxes in the three subbands. Figure 3 displays histograms of the net counts and fluxes in the 0.5–2.0 keV and 2–8 keV bands. Histograms of upper limits are also plotted, for sources that were detected in one band but not the other.

Finally, using custom code that was not part of ACIS Extract, we computed 90% uncertainties on the net counts in each band, through a Bayesian analysis of the Poisson statistics, with the simplifying assumption that the uncertainty on the background is negligible (Kraft et al. 1991). We used the net counts to compute the hardness ratios $(h - s)/(h + s)$, where h and s are the numbers of counts in the higher and lower energy bands, respectively. The resulting hardness ratios are bounded by -1 and +1. We defined a soft color using counts in the 2.0–3.3 keV and 0.5–2.0 keV bands ($HR0$), a medium color using counts in the 3.3–4.7 keV bands and 2.0–3.3 keV bands ($HR1$), and a hard color using counts in the 4.7–8.0 keV and 3.3–4.7 keV bands ($HR2$). We calculated uncertainties on the ratios using the 90% uncertainties on the net counts and Equation (1.31) in Lyons (1991; p. 26). The hardness ratios are listed in Table 3, and histograms showing their distributions are displayed in Figure 4.

The soft color, $HR0$, was used to distinguish foreground sources from objects that were likely to lie near or beyond the Galactic center. We select foreground X-ray sources as those with soft colors in the range $-1.0 \leqslant HR0 < -0.175$, which corresponds to absorption columns equivalent to $N_H \lesssim 4 \times 10^{22}$ cm^{-2}. Most of these should lie within 4 kpc of Earth (e.g., Marshall et al. 2006). We selected X-ray sources that were located near or beyond the Galactic center as those either that had soft colors $HR0 \geqslant -0.175$, or that were not detected in either of the 0.5–2.0 or 2.0–3.3 keV bands. This X-ray selection corresponds to absorption columns equivalent to $N_H \gtrsim 4 \times 10^{22}$ cm^{-2}. We find 2257 foreground X-ray sources, and 6760 sources near or beyond the Galactic center. Foreground and absorbed sources are plotted separately in Figure 4. Most absorbed sources do not have measured soft colors.

2.3. Variability

We searched for variability using the arrival times of the events. We searched for three kinds of variations: long-term variations that occurred between observations, short-term variability within individual observations, and periodic variability within individual observations.

2.3.1. Long-Term Variability

We searched for variations that occurred between observations by comparing the event-arrival times from all of the observations to a constant flux model using the KS statistic. Any source with a $< 0.1\%$ chance of being described by a constant flux model was considered to vary on long timescales. There were 856 sources that exhibited long-term variability, 137 of which also exhibited short-term variability. Therefore, about 10% of the sources vary on the day-to-month timescales between observations.

We characterized these long-term variations by computing the mean photon flux during each observation of a variable

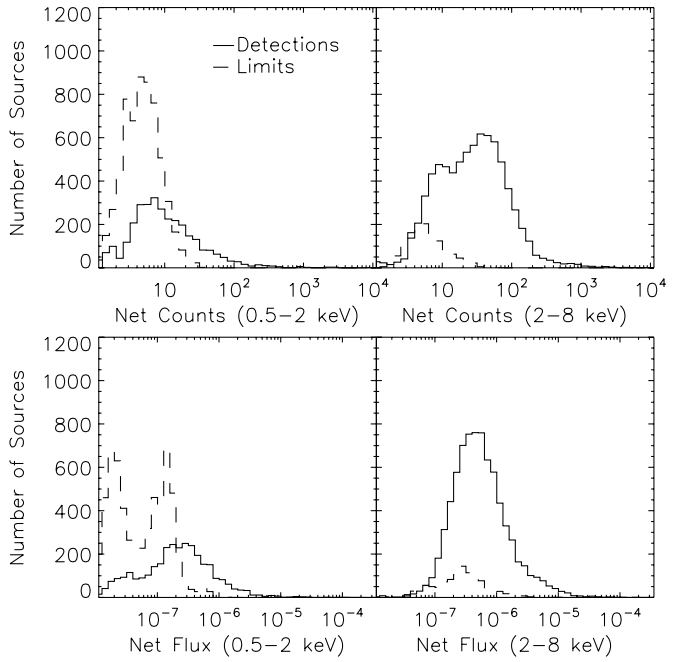

Figure 3. Top panels: distributions in net counts from individual sources. No corrections were applied to account for the exposure across the survey, which varies by a factor of 10. Values for the 0.5–2.0 keV band are plotted on the left, and for the 2–8 keV band on the right.Bottom panels: distribution of fluxes (photons cm^{-2} s^{-1}) from individual sources. The 0.5–2.0 keV fluxes were derived by dividing the net count rates by the effective area and exposure to the 0.5–2.0 keV band, whereas the 2–8 keV fluxes were computed by dividing the counts into into three energy bands (2.0–3.3 keV, 3.3–4.7 keV, and 4.7–8.0 keV), dividing by the respective effective areas and exposures, and summing the result. There are two peaks in each histogram, because the deeper observations were more sensitive to faint sources. In all panels, the solid lines are used for detections, and the dashed lines are 90% upper limits derived when a source was detected in one band, but not the other.

source. Table 4 lists the source name, observations in which the largest and the smallest fluxes were observed, the values of the largest and the smallest fluxes, and the ratios of those values. Figure 5 compares the amplitude of the variations to the maximum flux. In order to exclude measurements with poor signal-to-noise, the largest flux was defined as the measurement with the largest lower limit, and the smallest flux was defined as the measurement with the smallest upper limit. In most (740) cases, the smallest flux was consistent with zero, and the lower limits to the flux ratios were provided. In 224 cases, the uncertainties in the largest and the smallest fluxes overlapped, and the formal lower limit to the ratio was less than 1. The statistics on faint sources with low-amplitude variability tended to be poor, so Table 4 would be best used to identify highly variable sources for further study.

2.3.2. Short-Term Variability

We searched for variability within each observation by comparing the light curves to constant count rate models using the KS statistic. If the arrival times of events had a $< 0.1\%$ chance of being described by a uniform distribution, we considered a source to have short-term variability. We identified 294 sources, or 3% of our sample, as having clear short-term variations.

We roughly characterized the nature of the variability by dividing each time series into intervals that were consistent with having constant count rates, using the Bayesian Blocks algorithm of Scargle (1998). In brief, the algorithm compared

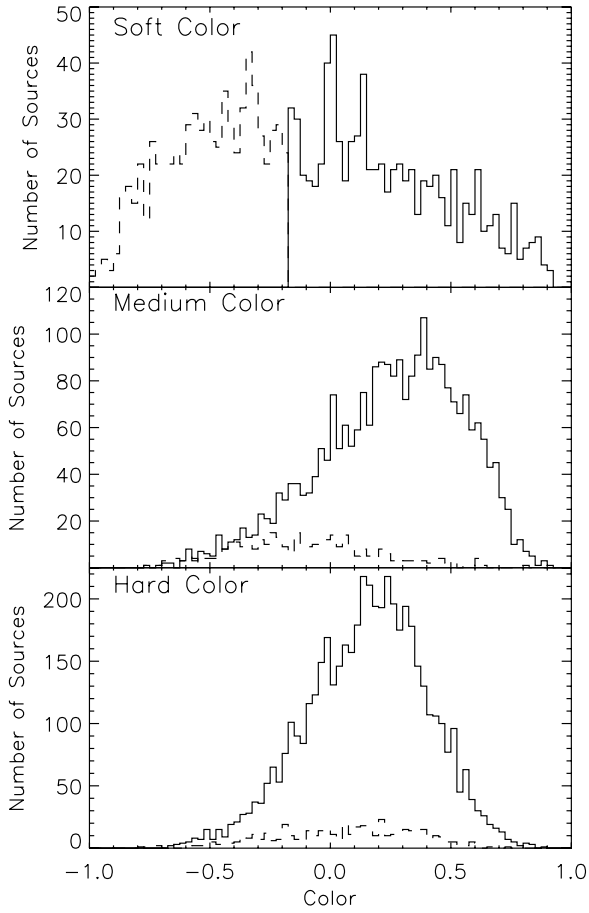

Figure 4. Distribution of measured hardness ratios, $(h-s)/(h+s)$, where h and s are the numbers of counts in the higher and lower energy bands, respectively. The top panel displays $HR0$, constructed from counts in the 2.0–3.3 keV and 0.5–2.0 keV bands; the middle panel displays $HR1$, using counts in the 3.3–4.7 keV and 2.0–3.3 keV bands; the bottom panel displays $HR2$, using counts in the 4.7–8.0 keV and 3.3–4.7 keV bands. Foreground sources are defined as those with $HRO < -0.175$, and are plotted with a dashed line. Galactic center sources have $HRO \geqslant -0.175$, and are plotted with a solid line. Most Galactic center sources do not have measured $HR0$, and their $HR1$ is skewed to higher values by absorption.

the probability that an interval could be described by two different count rates to the null hypothesis that the photons arrived with a single rate. If the ratio of the two probabilities exceeded a user-specified prior odds ratio, then the interval was divided at the time that produced two intervals with the largest calculated likelihood. This process was iterated until no subintervals were divided any further. We chose to apply the algorithm in order to describe each variable light curve with the fewest intervals with distinct rates (blocks). We applied three progressively looser odds ratios, successively demanding that the probability for the two-rate model exceed the null hypothesis by factors of 1000, 100, and 10 if the larger odds ratio failed to identify a change point. In this way, large flares were described with a few "blocks" using a large odds ratio, whereas small-amplitude variations were still characterized using a smaller odds ratio. This approach was deemed necessary in part because the Bayesian interpretation of the odds ratios does not have a good frequentist analog that could be compared to the probabilities returned by the KS test, and in part because the KS test and the Bayesian blocks tests are most sensitive to slightly different forms of variability. Ultimately, only 60% of the variable sources identified with the KS test were characterized with more than one block in the Bayesian block algorithm.

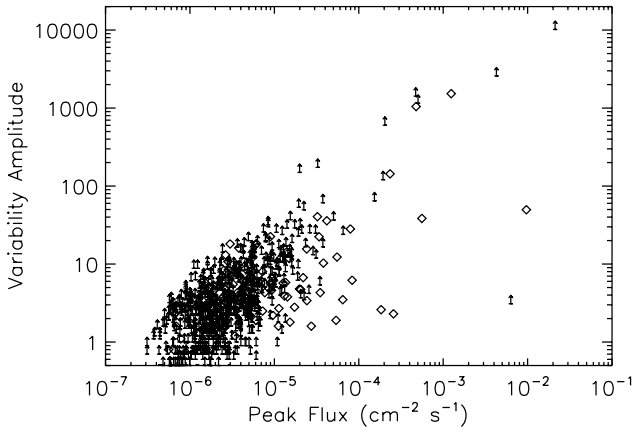

Figure 5. Summary of the properties of long-term variables. We plot the ratio of the maximum to minimum fluxes against the maximum flux. Measurements are represented with diamonds, and lower limits with upward-pointing arrows. The largest-amplitude variations necessarily have the largest peak fluxes, because the minimum fluxes generally represent nondetections, and are therefore equivalent to the sensitivity of our observations.

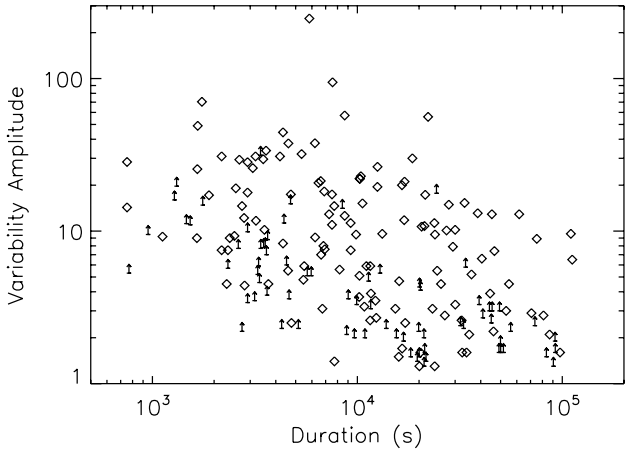

Figure 6. Summary of the properties of short-term variables, using parameters returned from the Bayesian blocks algorithm. We plot the ratio of the maximum to minimum fluxes against the duration of the peak-flux interval in an observation. Measurements are represented with diamonds, and lower limits with upward-pointing arrows. Low-amplitude variations are not represented among the short-duration events, because poor counting statistics prevents us from identifying them.

Despite the mismatch between the two tests, the characteristics of the variable sources identified by both the KS and the Bayesian blocks tests are illustrative. In Table 5, we list some properties of the variable sources: their names, the ObsIDs in which variability occurred, the odds ratio at which the Bayesian blocks algorithm identified a source as variable, the number of blocks used to describe the events, the durations of the brightest portions of the light curves, the minimum and the maximum fluxes, and the ratios of the maximum to minimum fluxes. Figure 6 compares the duration and amplitude of the variability. For 40% of the variable sources, the minimum flux was consistent with zero, so the ratio represents a lower limit to the variability amplitude. We find that all variations had timescales of >10 minutes. The amplitudes ranged from barely detectable 30% variations in the flux (CXOUGC J174534.8−290851), to one flare in which the flux increased by a factor of 250 (CXOUGC J174700.7−283205). Foreground sources are overrepresented among variable sources—they compose only 25% of our entire catalog, but 50% of the short-term variables—which is consistent with the expectation that they are nearby K and M dwarf flare stars (e.g., Laycock et al. 2005).

2.3.3. Periodic Variability

We searched for periodic variability in the brightest sources by adjusting the arrival times of their photons to the solar system barycenter and computing Fourier periodograms using the Rayleigh statistic (Bucceri et al. 1983). The individual X-ray events were recorded with a time resolution of 3.2 s, so the Nyquist frequency was ≈ 0.15 Hz, which represents the limit above which our sensitivity could not be well characterized. However, we computed the periodogram using a maximum frequency of ≈ 0.2 Hz, to take advantage of the limited sensitivity to higher frequency signals, and to ensure that any observed signal was not an alias.

We considered sources that, in individual observations, produced a large enough number of counts (N_γ) that a fully modulated signal could be detected with 99% confidence. The power $P_{\rm meas}$ required to ensure that a source had a chance $< 1 - C$ of being produced by white noise can be computed if one knows the number of trials in a search, ($N_{\rm trial}$), and is given by inverting $C \approx N_{\rm trial} e^{-P_{\rm meas}}$. Here, $P_{\rm meas}$ is normalized to have a mean value of 1, and the approximation is valid for $P_{\rm meas} \gg 1$ (Ransom et al. 2002). A count threshold can be determined by noting that, if background photons are negligible, the fractional root-mean-squared amplitude of a sinusoidal signal (A) is given by $A \approx (2P_{\rm meas}/N_\gamma)^{1/2}$. A fully modulated signal has $A = 0.71$. After iterating to determine the number of trials corresponding to each count limit, we found that a source with $N_\gamma = 86$ could be identified with $C = 0.99$ if it produced a fully modulated signal.

In total, we searched for pulsations in 717 event lists from 256 different sources, which required 2×10^7 trials. A single signal that had $C > 0.99$ given this number of trials must have had $P_{\rm meas} > 21.4$. However, multiple observations were searched for many sources, so we recorded signals with lower powers and checked whether they also appeared at the same frequency in other observations.

We identified two sources with periodic variability at $>$ 99% confidence, CXOUGC J174532.7−290550 and CXOUGC J174543.4−285841. We had previously identified both of these by combining 500 ks of exposure over the course of two weeks (Muno et al. 2003c). The other sources in Muno et al. (2003c) were too faint for their periodic variability to be identified in individual observations. We also identified a third source as a good candidate for having periodic variability, CXOUGC J174622.7−285218. Signals from this source were identified with periods of ≈ 1745 s in observation 4500 with $P_{\rm meas} = 10.9$ from 763 photons, and in observation 7048 with $P_{\rm meas} = 13.4$ from 310 photons (Figure 7). The joint probability that these signals were produced at the same frequency by noise (Ransom et al. 2002), given $N_{\rm trial} = 2 \times 10^7$, was only 1.4%. Periodic signals were neither detected from this source in observation 945 because the source fell on a chip edge, nor in observations 2273 and 2276 because their exposures were too short.

We refined our initial estimates of the period for CXOUGC J174622.7−285218 for each observation by computing pulse profiles from nonoverlapping 10^4 s intervals, and modeling the differences between the assumed and the measured phases using a first-order polynomial. The reference epochs of the pulse maxima for the two observations were 53165.3781(6) and 54145.1644(7) (MJD, Barycentric Dynamical Time). The best-fit periods were 1745 ± 3 s and 1734 ± 16 s for

Table 4
Sources with Long-Term Variability

Number	Name (CXOUGC J)	Location	Min. ObsID	$F_{\rm min}$ (10^{-7} cm^{-2} s^{-1})	Max. ObsId	$F_{\rm max}$ (10^{-7} cm^{-2} s^{-1})	$F{\rm max}/F_{\rm min}$
2	174457.4−285622	gc	5953	< 10	4684	31 ± 8	> 2.2
7	174500.6−290443	gc	7556	< 27	3392	14 ± 4	> 0.4
8	174501.3−285501	gc	4684	8 ± 6	1561a	12437 ± 166	1530^{+5824}_{-676}
12	174501.9−285719	f	2284	< 10	5953	16 ± 8	> 0.8
16	174502.5−290415	gc	2943	< 5	7556	64 ± 41	> 4.2
23	174504.2−285653	gc	4683	< 6	5953	16 ± 9	> 1.1
31	174504.8−285410	f	5951	< 16	6363	38 ± 14	> 1.5
35	174505.2−285713	f	2953	< 25	4683	16 ± 7	> 0.4
45	174506.1−285710	gc	5954	< 6	2953	26 ± 21	> 0.9
53	174507.0−290452	gc	6113	< 31	2953	29 ± 20	> 0.3
54	174507.1−285720	gc	5950	< 6	2951	21 ± 15	> 1.0
58	174507.5−285614	f	3665	< 12	6640	47 ± 44	> 0.3
71	174508.4−290033	f	3663	< 5	5360	375 ± 67	> 61.1
80	174509.2−285457	gc	2951	< 9	5954	20 ± 13	> 0.8
89	174509.5−285502	gc	3392	< 3	6363	19 ± 10	> 3.1
96	174510.1−285624	f	3549	< 6	1561a	16 ± 12	> 0.7
98	174510.2−285505	gc	3663	< 5	6642	51 ± 40	> 2.3
100	174510.3−290642	gc	7557	< 24	2954	55 ± 23	> 1.3
101	174510.4−285433	gc	4683	< 5	5953	19 ± 8	> 2.5
102	174510.4−285544	gc	5950	< 5	3665	11 ± 4	> 1.6
103	174510.4−285545	gc	5950	< 5	3665	12 ± 4	> 1.6
106	174510.6−285437	gc	3549	< 7	3663	14 ± 8	> 0.9
109	174510.8−285606	gc	6641	< 22	3665	12 ± 4	> 0.4
112	174510.9−285508	gc	5954	< 9	4683	18 ± 7	> 1.3
129	174511.6−285915	gc	5953	< 3	3392	8 ± 2	> 1.6
143	174512.1−290005	gc	2952	< 7	3393	15 ± 3	> 1.6
155	174512.4−285318	gc	7555	< 27	3393	11 ± 4	> 0.3
164	174512.8−285441	gc	6644	< 22	2953	33 ± 20	> 0.6
191	174514.1−285426	gc	5953	< 7	5954	55 ± 20	> 4.7
226	174515.1−290006	gc	4684	< 3	3392	10 ± 2	> 2.8

Notes. The columns of the table are: the record number from Table 2, the source name, a flag stating whether a source is in the foreground or near the Galactic center, the ObsID in which the minimum flux was observed, the minimum flux, the ObsID in which the maximum flux was observed, the maximum flux, and the ratio of the maximum to minimum fluxes.

(This table is available in its entirety in a machine-readable form in the online journal. A portion is shown here for guidance regarding its form and content.)

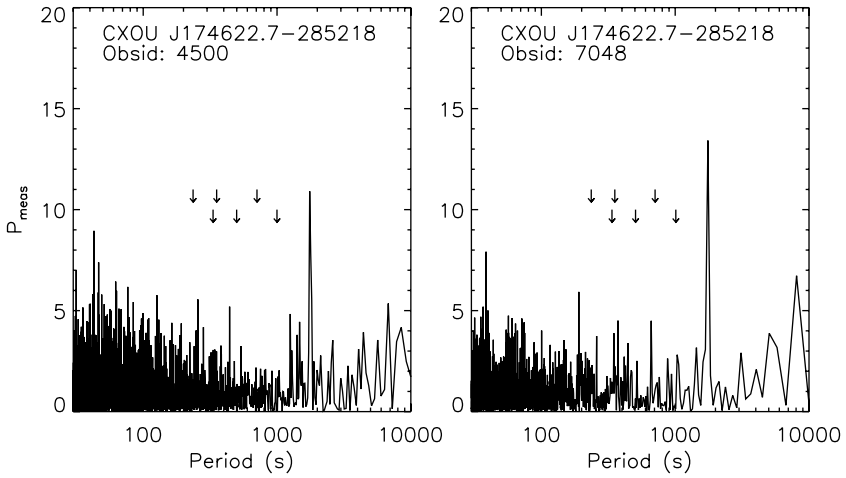

Figure 7. Fourier periodograms for the two observations in which a 1745 s signal was detected from CXOUGC J174622.7−285218. The signal has a joint probability of 1.4% of resulting from white noise, given $N_{\rm trial} = 2 \times 10^7$. The downward-pointing arrows show the fundamental and first two harmonics of the periods with which the satellite point was dithered in pitch and yaw.

observations 4500 and 7048, respectively. The pulse profiles for each observation are displayed in Figure 8. The fractional rms amplitudes of the pulsations were 21% and 32%, respectively. Given the long period for this source, it is most likely a magnetically accreting white dwarf (Muno et al. 2003c).

2.4. Sensitivity

We calculated the sensitivity of our observations using synthetic star tests, following the basic methods described in Bauer et al. (2004) and Muno et al. (2006a; see Wang 2004 for another approach). We generated maps of our sensitivity both for each of

Table 5
Sources with Short-Term Variability

Number	Name (CXOUGC J)	Location	ObsID	Prior Odds	$N_{\rm blocks}$	$T_{\rm peak}$ (s)	$F_{\rm min}$ (10^{-7} photons cm^{-2} s^{-1})	$F_{\rm max}$	$F{\rm max}/F_{\rm min}$
1	174457.1−285740	f	1561b	100	2	3152	< 17	193^{+72}_{-55}	> 3.3
3	174459.1−290604	gc	3663	10	2	19600	< 11	48^{+17}_{-15}	> 1.4
71	174508.4−290033	f	5360	1000	2	2736	< 63	673^{+119}_{-103}	> 1.6
186	174513.7−285638	gc	4684	10	2	21312	< 7	36^{+12}_{-9}	> 1.4
257	174516.6−285412	f	4684	1000	2	16512	5^{+7}_{-4}	90^{+23}_{-19}	20.0 ± 24.4
304	174517.8−290653	gc	3392	1000	2	110160	4^{+5}_{-4}	40^{+6}_{-5}	9.6 ± 10.5
364	174519.5−285955	gc	4683	10	2	6896	3^{+3}_{-2}	57^{+26}_{-19}	18.2 ± 18.0
398	174520.3−290143	gc	2943	1000	2	3472	5^{+5}_{-3}	134^{+58}_{-42}	29.6 ± 29.0
424	174520.6−290152	f	3392	1000	5	33360	34^{+6}_{-5}	526^{+35}_{-33}	15.3 ± 2.7
424			3393	1000	4	22144	15^{+3}_{-3}	858^{+55}_{-52}	56.1 ± 11.0
424			5951	1000	2	23760	9^{+8}_{-5}	104^{+17}_{-15}	11.3 ± 8.2
470	174521.7−290151	gc	5950	100	2	10400	2^{+4}_{-2}	52^{+19}_{-15}	22.9 ± 30.4
472	174521.8−285912	f	3392	1000	3	18560	3^{+3}_{-2}	103^{+17}_{-15}	30.0 ± 21.6
663	174525.1−285703	f	3665	1000	2	1664	12^{+4}_{-3}	566^{+176}_{-137}	49.0 ± 20.6
811	174527.1−290730	gc	3549	10	2	3296	< 6	87^{+57}_{-38}	> 5.9
1100	174530.3−290341	gc	3392	1000	3	21440	5^{+8}_{-5}	91^{+15}_{-13}	17.3 ± 20.5
1100			5950	1000	2	17120	55^{+9}_{-8}	136^{+20}_{-17}	2.5 ± 0.5
1183	174531.1−290219	gc	3393	10	2	70704	8^{+3}_{-2}	25^{+4}_{-4}	2.9 ± 1.0
1525	174534.2−290011	f	3392	100	2	49392	< 1	14^{+4}_{-3}	> 2.7
1569	174534.5−290236	gc	3392	1000	2	73504	< 1	10^{+5}_{-2}	> 2.4
1608	174534.8−290851	f	1561a	100	2	21168	< 11	78^{+17}_{-14}	> 1.3
1676	174535.5−290124	gc	3549	1000	2	15920	1234^{+77}_{-73}	1877^{+71}_{-68}	1.5 ± 0.1
1676			5950	100	2	16544	156^{+14}_{-13}	267^{+27}_{-24}	1.7 ± 0.2
1676			6644	1000	2	2304	179^{+78}_{-57}	809^{+155}_{-131}	4.5 ± 1.9
1686	174535.6−290133	gc	3665	1000	3	61632	14^{+6}_{-4}	178^{+15}_{-14}	12.9 ± 5.0
1686			6641	1000	2	4336	650^{+238}_{-183}	5389^{+222}_{-213}	8.3 ± 2.7
1691	174535.7−285357	f	5951	100	2	29264	10^{+11}_{-8}	79^{+13}_{-12}	7.9 ± 7.5
1706	174535.8−290159	gc	3393	1000	2	90464	< 3	14^{+3}_{-3}	> 0.8
1748	174536.1−290806	gc	3393	1000	2	75104	3^{+4}_{-3}	31^{+6}_{-5}	8.9 ± 9.3
1765	174536.3−285545	f	3392	100	4	7568	3^{+2}_{-1}	252^{+81}_{-63}	94.5 ± 60.5

Notes. The columns of the table are: the record number from Table 2, the source name, a flag stating whether a source is in the foreground or near the Galactic center, the ObsID in which the variability was identified, the odds ratio used as a prior in the Bayesian blocks routine when characterizing the variability, the number of blocks used to describe the data, the duration of the block with the maximum flux, the minimum flux, the maximum flux, and the ratio of the maximum to minimum fluxes. The table only includes variable sources that were successfully characterized by the Bayesian blocks routine.

(This table is available in its entirety in a machine-readable form in the online journal. A portion is shown here for guidance regarding its form and content.)

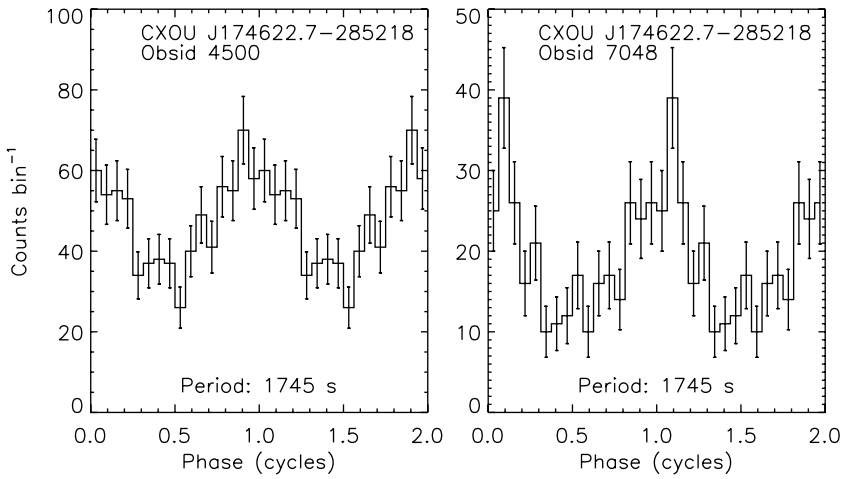

Figure 8. Pulse profiles for the two observations in which the 1745 s signal was detected from CXOUGC J174622.7−285218. Two identical cycles have been displayed in each panel. The profiles are consistent with sinusoids, within their uncertainties.

the stacked observations (i.e., centered on ObsIDs 3392, 4500, 5892, 7034–7048, and 944), and for a fiducial field with an exposure time of 12 ks for those regions only covered by the shallow exposures of Wang et al. (2002a). In brief, for each pointing,

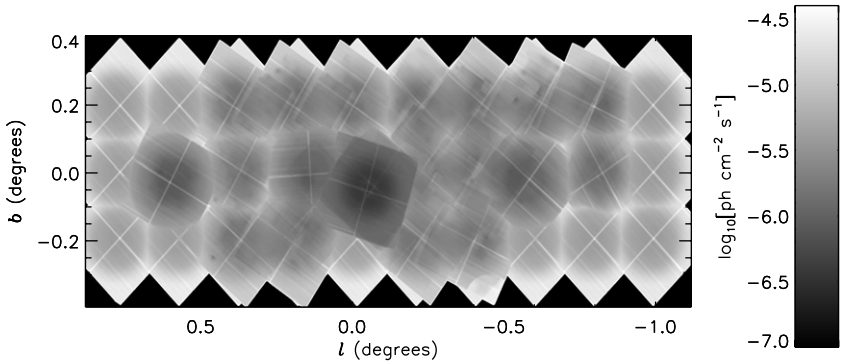

Figure 9. Map of the limiting flux for our survey. Sources brighter than the limiting flux at each point have a > 90% chance of being detected.

we generated a background map by (1) removing events from within a circle circumscribing ≈ 90% of the energy of the PSF around each detected source, and then (2) filling the "holes" in the image with numbers of counts drawn from Poisson distributions with means equal to those of surrounding annuli. We then simulated 100 star fields per pointing. We placed ≈ 5000 point sources at random positions in each background image, with fluxes distributed as $N(>S) \propto S^{-\alpha}$ with a slope $\alpha = 1.5$, and minimum fluxes that would produce three counts in a 100 ks exposure. We converted these fluxes to expected values for the numbers of counts using an exposure map. The exposure map was normalized to produce the mean flux-to-counts conversion for X-ray sources located at or beyond the Galactic center ($HR0 > -0.175$; Muno et al. 2006a).[26] Then, to account for the Eddington bias, we drew observed numbers of counts from Poisson distributions with mean values equal to the expected counts. Next, we obtained model images of the PSF from the routine `mkpsf`, averaged them when appropriate, and used the composite PSF as the probability distribution to simulate the two-dimensional image of the counts. These were added to the synthetic exposure. Finally, we searched the synthetic image for point sources using `wavdetect` for the 12 ks exposures, and `wvdecomp` for the stacked observations. By comparing the input and the output lists, we estimated the minimum flux at which a source would be detected in 50% and 90% of the trials over a grid of points covering our survey. We interpolated between these points to make a map of the sensitivity for each image.

None of our observations are formally confusion-limited at our completeness limits (Hogg 2001; see also Muno et al. 2003). If the background diffuse X-ray emission are unresolved stellar sources, then confusion caused by undetected sources is accounted for naturally by our background maps.

In order to produce a global sensitivity map, we combined the sensitivity maps from the above simulations by recording the best sensitivity at each point in the image. The map of 90% confidence limits is displayed in Figure 9. The effective area of the survey as a function of limiting photon flux and luminosity is displayed in Figure 10. We are sensitive to $\approx 4 \times 10^{32}$ erg s^{-1} (0.5–8.0 keV, assuming $D = 8$ kpc) at 90% confidence over 1 deg^2, and to $\approx 1 \times 10^{32}$ erg s^{-1} over 0.1 deg^2. This is a factor of ≈ 2 improvement over Muno et al. (2006a).

However, we still find that the majority of X-ray sources are detected at fluxes below our completeness limits. Of the 6760 sources that are likely to lie at or beyond the Galactic center ($HR0 > -0.175$), only 15% are brighter than the 90% completeness limit at the point at which they were detected, and only 40% are brighter than the 50% completeness limit. This is caused by two effects. First, 20% of the sources are detected only in the hard band, whereas our completeness limits are for the full band. Second, the number-flux distribution is steep (Section 3.3), such that many of the faint sources are only detected because of positive Poisson fluctuations in their count rates.

These maps are used in selecting complete samples of sources for measuring the spatial (Section 3.2) and flux (Section 3.3) distributions. Sources below our completeness limits are still securely detected, although other sources with similar intrinsic fluxes have been missed.

2.5. *Refined Source Positions*

Experience with matching X-ray and optical sources as part of the Chandra Deep Fields and Orion Ultradeep projects suggests that the positions of the X-ray sources can be refined with respect to those provided by the wavelet algorithms (Alexander et al. 2003; Getman et al. 2005). Therefore, we used the implementations of their techniques in ACIS Extract to refine the positions of our sources. For each source, we made a composite image by combining the event lists from each relevant observation, and then made a matching composite PSF image that we weighted by the values of the exposure maps at the source positions. From this image, we computed two additional estimates for the source position: the mean positions of the events within each source region, and a centroid determined by cross-correlating the PSF and the source images. Following Getman et al. (2005), if a source lay within 5′ of the aim point, we used the mean position of the events within the source extraction region. If the source lay beyond 5′, we used the position determined by cross-correlating the source image and the PSF image. However, if the offset of the refined position from the wavelet position was larger than the smallest source extraction radius that we used, we assumed that a nearby source had caused confusion, and retained the wavelet position.

Unfortunately, we could not empirically calibrate the uncertainties on our source positions, because even the foreground infrared sources had such a high density that ≈ 50% of those that fell within 3″ of an X-ray source were chance alignments. Therefore, we computed 95% positional uncertainties using Equation (5) in Hong et al. (2005a),[27] which is based on the positions of

[26] We note that in Muno et al. (2006a), we calculated flux limits from a monoenergetic exposure map that overestimated the effective area by 50%, which caused us to report limiting fluxes that were erroneously low.

[27] This differs from the equation we used for eliminating duplicates, because that step was implemented much earlier in the process of producing the catalog, before we had settled on a final uncertainty estimate. The difference has no practical impact on the catalog.

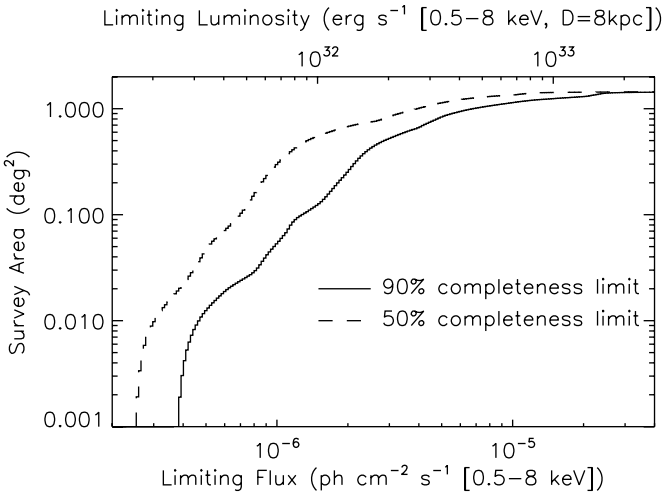

Figure 10. Area over which we were sensitive to sources of given fluxes (bottom axis) and luminosities (top axis, assuming $D = 8$ kpc, a $\Gamma = 0.5$ power-law spectrum, and $N_{\rm H} = 6 \times 10^{22}$ cm^{-2}), with 50% and 90% confidence.

sources reported by `wavdetect` in simulated observations,

$$r_{\rm err} = 0\farcs25 + \frac{0\farcs1}{\log_{10}(c+1)}\left[1 + \frac{1}{\log_{10}(c+1)}\right] + 0\farcs03\left[\frac{\theta}{\log_{10}(c+2)}\right]^2 + 0\farcs0006\left[\frac{\theta}{\log_{10}(c+3)}\right]^4. \quad (1)$$

Here, θ is the offset in arcminutes of the source from the nominal aim point, and c is the net number of counts. For sources detected in composite images, we defined c to be the net counts summed over all observations, and θ to be the exposure-weighted averages of the sources' offsets from the aim points of their respective observations. For sources detected in individual observations, we defined c and θ to be the values for the observations in which the sources were identified.

If $r_{\rm err}$ is larger than the smallest radius of the region used to extract photometry for the source (the "source radius"), the uncertainty was set equal to the radius of the extraction region. These sources are marginally detected, and the high background in the Galactic center produces a large tail in the distribution of possible positions. We retained them because they passed all of our other selection criteria.

Hong et al. (2005a) established Equation (1) by running `wavdetect` on simulated, single observations that were generated using a ray-tracing code. Unfortunately, our observations are more complicated. On the one hand, most of the positions are determined from composite images generated from observations with very different aim points. The inclusion of data with large θ could add uncertainty to our measurements. On the other hand, our positions have been refined compared to the `wavdetect` values, so the uncertainty on some sources could be smaller. Therefore, we view Equation (1) as a compromise. Nonetheless, a comparison of the offsets between 500 foreground X-ray sources and the blue 2MASS sources that are their counterparts (as described in detail in J. Mauerhan et al., in preparation) reveals that the positions in the new catalog are $\approx 60\%$ better than in Muno et al. (2003a, 2006a).

We also note that because of the way we averaged the PSF, the positions and uncertainties for the sources that vary in flux between observations (10% of our sample) could be misestimated. For example, a variable source that was only bright in an off-axis observation would have a larger uncertainty than might be expected if it were also bright during an on-axis observation. We have not evaluated whether systematic offsets in the positions are expected.

2.6. Details of the Tables

Table 2 contains the locations of the point sources, parameters related to the observations of each source, and information on the data quality. Its columns are as follows.

1. Record locators that can be used to cross-correlate with other tables.
2. The source names, which are derived from the coordinates of the source based on the IAU format, in which least-significant figures are *truncated* (as opposed to rounded). The names should not be used as the locations of the sources.
3. The right ascensions and declinations of the sources, in degrees (J2000).
4. Same as column 3.
5. The 95% uncertainties in the positions (the error circles). There are 5810 sources with uncertainties $\leqslant 1''$ (half of which are within $7'$ of Sgr A*), and 1950 with uncertainties $\leqslant 0\farcs5$ (85% of which are within $7'$ of Sgr A*).
6. Flag indicating how the positions were derived. A "d" indicates that the position is from the mean position of events, a "c" indicates that it was derived by cross-correlating the image and the PSF, and a "w" indicates that it was derived from a wavelet algorithm. Sources marked with a "w" are likely to be confused with a nearby source, or in a region of high background.
7. The images in which the sources were identified. The tags "full," "2002," "2004," and "2005" indicate that a source was found in composite images of the Sgr A* field. All other values are the observations in which a source was detected. Two sources added manually are tagged with "hand."
8. Additional information about how the sources were detected. The tag "full" refers to any source detected with `wavdetect` in the 0.5–8.0 keV band; "soft" sources were detected in the 0.5–2.0 keV but not the full band; "hard" sources were detected in the 4–8 keV band but neither of the other two bands. The tag "tile" indicates that the source was detected in a composite 0.5–8.0 keV image with `wvdecomp`.
9. The offsets (θ) from the aim point, in arcmin. If a source position was estimated from a composite image, θ is the mean offset weighted by the exposure. If a position was taken from a single observation, θ is the offset for that observation.
10. The number of observations used to compute the photometry for each source.
11. The exposure times in seconds.
12. The fractions of the PSF enclosed by the source extraction regions.
13. The fiducial energies of the PSFs used to construct the source extraction regions.
14. The smallest radius for the extraction region that was used for a source, in arcseconds. This is determined from the observation in which the source was closest to the aim point. It is also an absolute upper bound to the positional uncertainty for a source.
15. The 50% completeness limit at the position of the source. Sources brighter than these completeness limits can be used to compute spatial and flux distributions, although the sensitivity map (Figure 9) is needed to compute the corresponding survey area.

16. Flags denoting quality, and other information: "a" for sources used to register the astrometry of fields; "s" for sources variable on short timescales, as indicated by probabilities of $< 0.1\%$ that the event-arrival times for at least one observation were consistent with a uniform distribution according to the KS test; "l" for sources that were variable on long timescales, as indicated by a probability of $< 0.1\%$ that the fluxes for all observations were consistent with a uniform distribution according to the KS test; "e" for sources that may be part of an extended, diffuse feature (Muno et al. 2004a); "c" for sources confused with another nearby source; "g" for sources that fell near the edge of a detector in one or more observations; "b" for sources for which the source and the background spectra have a $> 10\%$ chance of being drawn from the same distribution according to a KS test; "x" for sources for which the 0.5–2.0 keV band photometry is inaccurate because the satellite was programmed to omit photons below 1 keV from the telemetry; and "p" for sources that suffered from photon pile-up.

Table 3 contains the X-ray photometry for each source. It contains the following columns.

1. The record locators.
2. The source names.
3. The log of the probabilities that the source and the background spectra are derived from the same distribution, according to a KS test. Large negative values indicate that the source and the background spectra are distinct, and therefore that the source is most likely real.
4. The total numbers of counts in the 0.5–2.0 keV band.
5. The estimated numbers of background counts in the 0.5–2.0 keV band.
6. The net numbers of counts in the 0.5–2.0 keV band, and the 90% lower and upper uncertainties. In the case of nondetections, an upper limit is provided.
7. The total numbers of counts in the 2–8 keV band.
8. The estimated numbers of background counts in the 2–8 keV band.
9. The net numbers of counts in the 2–8 keV band, and the 90% lower and upper uncertainties. In the case of nondetections, an upper limit is provided.
10. The fluxes in the 0.5–2.0 keV band, in units of photons $\mathrm{cm}^{-2}\ \mathrm{s}^{-1}$.
11. The fluxes in the 2–8 keV band, in units of photons $\mathrm{cm}^{-2}\ \mathrm{s}^{-1}$.
12. The mean energy of photons in the source region, statistically corrected for the background.
13. The soft colors and 90% upper and lower uncertainties.
14. The medium colors and 90% upper and lower uncertainties.
15. The hard colors and 90% upper and lower uncertainties.

These tables were designed to be inclusive, so sources of questionable quality are included. For instance, 134 sources have net numbers of counts in the 0.5–8.0 keV band that are consistent with 0 at the 90% confidence level. These sources are only detected in a single band and are presumably either very hard or very soft, detected in single observations because they were transients, or detected in stacked observations with `wvdecomp` at marginal significance. We have chosen to include them because they passed the test based on Poisson statistics from Weisskopf et al. (2007).

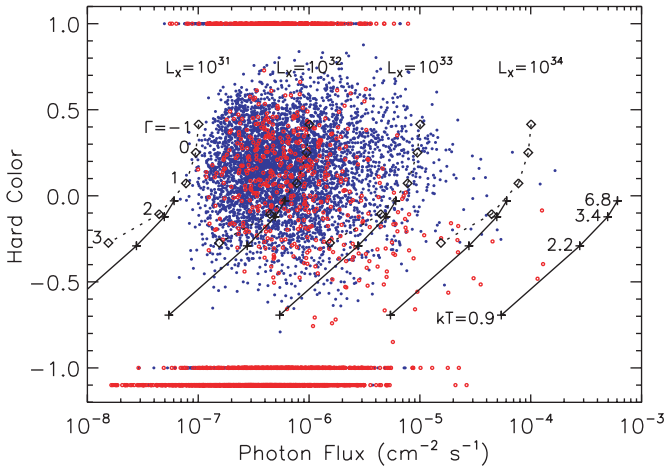

Figure 11. Hard color plotted against the photon flux from each source. Foreground sources are plotted as open red circles, and Galactic center sources as filled blue circles. Sources detected only in the 3.3–4.7 keV band are assigned hard colors of -1; those only detected in the 4.7–8.0 keV band are assigned $HR2 = +1$, and those detected in neither of the bands are assigned $HR2 = -1.1$. We have also plotted the colors expected for sources of varying luminosities at a distance of 8 kpc, and absorbed by $6 \times 10^{22}\ \mathrm{cm}^{-2}$ of interstellar gas and dust. The dotted lines are for power-law spectra, and the solid lines for thermal plasma spectra.

3. RESULTS

With a catalog of X-ray sources and associated maps of our sensitivity, it is straightforward to examine the flux and spatial distributions of our sources. We have previously reported these quantities based on the catalogs produced for the central 20 pc around Sgr A* (Muno et al. 2003a) and on the wide, shallow survey data that were in the archive as of 2005 June (Muno et al. 2006a). Here, we derive these quantities for the new catalog, and briefly compare the distributions to recent results from Koyama et al. (2007) on the distribution of diffuse iron emission.

3.1. X-Ray Colors and Intensity

In Figure 11, we plot the hard color versus the flux from each source. Foreground sources are indicated with open red circles, and sources at or beyond the Galactic center with filled blue circles. There are 6381 Galactic center sources and 1091 foreground sources with measured hard colors. We have calculated the hardness ratios and photon fluxes that we would expect to get from these energy bands for a variety of spectra and 0.5–8.0 keV luminosities using `PIMMS` and `XSPEC`. In Figure 11, we plot the colors and fluxes expected for power-law spectra with the dotted lines, and for a optically thin thermal plasma with the solid lines. We have assumed a distance of 8 kpc and $6 \times 10^{22}\ \mathrm{cm}^{-2}$ of absorption from interstellar gas and dust.

The median hard color for the Galactic center sources is 0.17. For interstellar absorption, this corresponds to a $\Gamma \approx 0.5$ power law. Using a simulated spectrum, we have determined that the photon fluxes can be converted to energy fluxes according to 1 photons $\mathrm{cm}^{-2}\ \mathrm{s}^{-1} = 8.7 \times 10^{-9}\ \mathrm{erg\ cm}^{-2}\ \mathrm{s}^{-1}$ (0.5–8.0 keV). The deabsorbed 0.5–8.0 keV flux is approximately 1.7 times larger, so that for a distance $D = 8$ kpc, $10^{34}\ \mathrm{erg\ s}^{-1}$ equals 9×10^{-5} photons $\mathrm{cm}^{-2}\ \mathrm{s}^{-1}$. The large median value of the hard color is inconsistent with that expected from a thermal plasma (of any temperature) attenuated by interstellar gas and dust. However, our earlier study of the spectra of brighter sources suggest that intrinsic absorption is present, and that the underlying spectrum is consistent with a $kT = 7$–9 keV thermal plasma

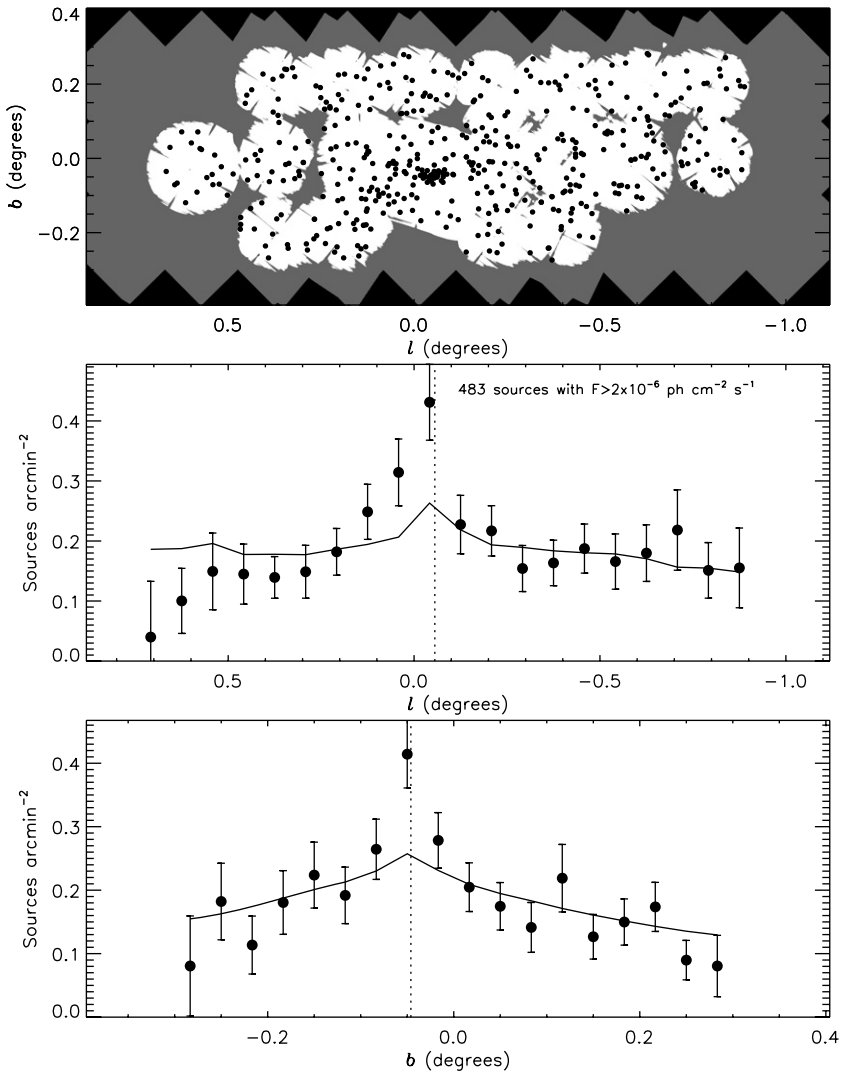

Figure 12. Spatial distribution of point sources that are securely detected, with fluxes $> 2 \times 10^{-6}$ photons cm^{-2} s^{-1} (0.5–8.0 keV), and that lie near or beyond the Galactic center ($HR0 > -0.175$). In the top panel, we show the two-dimensional distribution. Over much of the region, we are less sensitive than our nominal limit, so we have indicated these regions with grey. Regions in which we were more sensitive are in white, and the detected sources are indicated with filled black circles. Middle panel: histogram of the number of sources per square arcminute, computed as a function of Galactic longitude. The area used to normalize the histogram is derived from the white area in the panel above. The solid line illustrates the model stellar distribution from Launhardt et al. (2002) and Kent et al. (1991), which originally was derived from infrared observations. The model distribution was also computed for the white area in the top panel. Bottom panel: same as for the middle panel, except that the source distribution is plotted as a function of Galactic latitude.

(Muno et al. 2004b). For sources that are intrinsically absorbed, the luminosities will be significantly higher than implied by Figure 11.

3.2. Spatial Distribution

We present the spatial distribution of X-ray sources located near or beyond the Galactic center ($HR0 > -0.175$) in Figure 12. We examined only sources brighter than 2×10^{-6} photons cm^{-2} s^{-1}, and only included a source if the 50% confidence flux limit at its position was less than or equal to 2×10^{-6} photons cm^{-2} s^{-1}. This flux limit was chosen as a compromise between the area over which the distribution is derived, which decreases for lower flux limits (Figure 9), and the number of sources used in the distribution, which tends to increase for lower flux limits (Figure 3). In the top panel of Figure 12, we display the locations of each of the 479 sources that met the flux criteria. The area over which the flux limit is $< 2 \times 10^{-6}$ photons cm^{-2} s^{-1} is displayed in white, and the greyed areas indicate regions of poorer sensitivity. A concentration of X-ray sources is evident near the position of Sgr A*. In the bottom panels of Figure 12, we display histograms of the numbers of sources per unit area, as functions of Galactic longitude and latitude. Only regions of good sensitivity are used.

We then compared the spatial distributions to that of the stellar mass that has been inferred from infrared observations. Our mass model consists of the young nuclear bulge and cusp and the old Galactic bulge from Launhardt et al. (2002), and the model for the Galactic disk from Kent et al. (1991; see Muno et al. 2006a for further details). To make a direct comparison with our unevenly sampled spatial distributions, we integrated the model for the stellar mass from 6 to 14 kpc along the line of sight at points on a 1′ grid covering our survey region, and interpolated the resulting values onto the image. We then summed the values of the integrated mass over areas of good sensitivity, to match the longitude and latitude bins of the observed histogram. Finally, we minimized chi-squared over one parameter to scale the binned mass model to the observed distributions of X-ray sources. We find a best-fit scaling factor

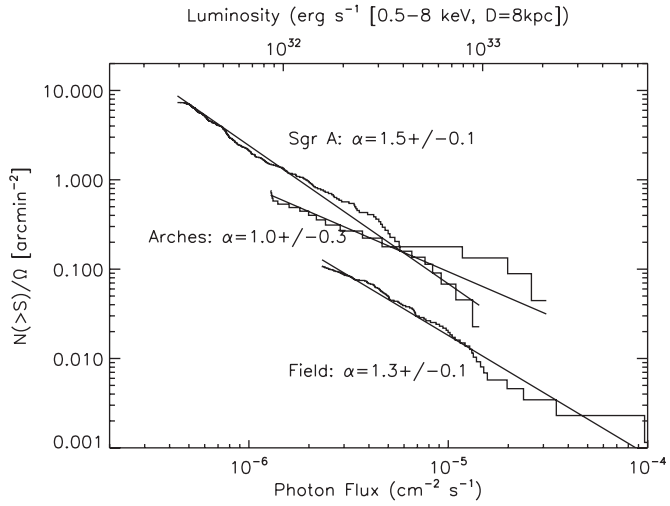

Figure 13. Cumulative number of sources as a function of limiting flux, for three regions of interest: the inner 8′ radius around Sgr A*, the 8′ radius around the Arches cluster (excluding the overlap with the Sgr A* region), and the wide survey (excluding the fields around Sgr B, Sgr C, the Arches, and Sgr A*). The solid line indicates the best-fit power law, which we determined from the unbinned distribution. The top axis provides an estimate of the luminosity corresponding to the observed flux. The luminosity is calculated assuming $D =$ 8 kpc and a mean photon energy of 8.7×10^{-9} erg (corresponding to a $\Gamma = =$ 0.5 power law absorbed by $N_{\rm H} = 6 \times 10^{22}$ cm^{-2}).

of 5×10^{-7} X-ray sources per solar mass for sources brighter than 2×10^{-6} photons cm^{-2} s^{-1} for both the latitude and the longitude distributions. For the longitude distribution, $\chi^2/\nu =$ 22.4/19, and for the latitude distribution, $\chi^2/\nu = 20.6/17$. The best-fit models are displayed with solid lines in the bottom panels of Figure 12.

The models are acceptable descriptions of the data. However, in the plot as a function of longitude, at the inner few arcminutes around Sgr A*, and just to the east toward the Arches and the Quintuplet regions, there is an $\approx 2.8\sigma$ excess in the number of observed X-ray sources. We find that this excess is also present with similar significance if we chose tighter or looser flux limits between 1 and 5×10^{-6} photons cm^{-2} s^{-1}. The model also predicts more sources than observed at $L = 0.^\circ5$–$0.^\circ6$ at the 1σ level, but this is probably because the Sgr B molecular complex attenuates X-rays from sources behind it.

3.3. Number-Flux Distribution

We computed the number-flux distribution based on the maximum-likelihood algorithm described in Murdoch et al. (1973), which we modified to use Poisson statistics in the manner described in Appendix B of Muno et al. (2006a). We examined three regions that had well defined flux limits and effective exposure times: the inner 8′ around Sgr A*, the 8′ around the Arches cluster (excluding the overlap with the Sgr A* field), and the portions of the survey covered by the 40 ks pointings taken between 2006 and 2007. We assumed that the number-flux distribution was a single power law over the ranges of fluxes that we measured, $N(>S) = N_0(S/S_0)^{-\alpha}$. We display the resulting cumulative number-flux distributions in Figure 13, and list the best-fit parameters in Table 6. Our distributions extend a factor of ≈ 2 deeper than in Muno et al. (2006a).

The fit to the distribution from the Sgr A* region is formally poor, because the distribution steepens at low fluxes (Muno et al. 2003a). However, we do find that the Arches region has a flatter flux distribution ($\alpha = 1.0 \pm 0.3$) than either the inner 8′ around Sgr A (1.55 ± 0.09) or the wide survey field (1.3 ± 0.1). The difference is only significant at the 1.4σ level. Nonetheless, given that there are also excess sources coincident with the Arches region in the spatial distribution, we suggest that there is a genuine overabundance of bright X-ray sources in this region of recent star formation.

Table 6
Parameters of the $\log N - \log S$ Distribution

Field	$S_{\rm lim}$ 10^{-6} photons cm^{-2} s^{-1}	Num. Sources	Area (arcmin^2)	α	N_0 (arcmin^{-2})	$P_{\rm KS}$
Sgr A*	0.5	323	44	1.55 ± 0.09	0.41	0.00
Arches	1	17	22	1.0 ± 0.3	0.08	0.88
Field	3	92	813	1.3 ± 0.1	0.02	0.88

Notes. The normalization of the $\log N - \log S$ distribution, N_0 is listed for a fiducial flux of 2×10^{-6} photons cm^{-2} s^{-1}, to match the spatial distribution in Figure 4. $P_{\rm KS}$ represents the probability under a Kolgoromov–Smirnov test of seeing the observed difference between the observed and the model distribution assuming that they are identical, so that very small values would indicate a poorer match.

A similar asymmetry has been identified in the flux of diffuse emission from helium-like iron (Koyama et al. 2007). We suggest that both the excess point sources and the excess iron emission are related to the concentration of young stars in this region, the most dramatic manifestations of which are the Arches and the Quintuplet clusters (e.g., Figer et al. 1999). The iron emission is probably diffuse, hot plasma that forms in shocks where the stellar winds from the clusters impact the interstellar medium (ISM; 2002, 2004, 2006). The excess point sources are probably young, OB and Wolf–Rayet stars in binaries (e.g., Mauerhan et al. 2007).

4. DISCUSSION

We have presented a catalog of 9017 X-ray sources located in the inner $2^\circ \times 0.^\circ8$ around the Galactic center. This increases the number of sources known in the region by a factor of 2.5. For all of the sources, we provide tables listing their positions (Table 2), photometry, and colors (Table 3). Of these sources, 6760 have hard colors that are consistent with high absorption columns $N_{\rm H} \gtrsim 4 \times 10^{22}$ cm^{-2}, which indicates that they lie at or beyond the Galactic center. In addition, the positions of the X-ray sources in this catalog are more accurate than earlier versions. This catalog contains 2029 sources with $< 0.''5$ uncertainties (90% confidence), and another 3981 with uncertainties between $0.''5$ and $1''$. This catalog will be excellent for comparisons with multiwavelength ones, in order to search for young stars, high-mass X-ray binaries, and pulsars (e.g., Wang et al. 2002b; Lu et al. 2003; Mikles et al. 2006; Muno et al. 2006b; Mauerhan et al. 2007).

The luminosity range that we cover, from 10^{31} to 10^{34} erg s^{-1} (0.5–8.0 keV; assuming a $\Gamma = 1.5$ power law, $N_{\rm H} = 6 \times 10^{22}$ cm^{-2}, and $D = 8$ kpc), is at least an order of magnitude fainter than studies of Local Group galaxies (e.g., Trudolyubov & Priedhorsky 2004; Kilgard et al. 2005; Plucinsky et al. 2008). Consequently, the nature of the sources that we study are also very different. Whereas the detectable stellar population of external galaxies in X-rays is dominated by accreting black holes and neutron stars, most of our sources are probably cataclysmic variables (e.g., Muno et al. 2006a). The hardness of the X-ray colors (Figure 11) suggests that the sources are specifically magnetically accreting white dwarfs (Ezuka & Ishida 1999; Muno et al. 2006a). Therefore, the X-ray population probably represents old stars. Indeed, the spatial distribution

Table 7
Luminous X-Ray Binaries Covered by Our Observations

Chandra name (CXOUGC J)	Common Name	RA (Degrees, J2000)	DEC (Degrees, J2000)	Uncertainty (arcsec)	Reference
174354.8−294441	1E 1740.7-2942	265.97864	−29.74499	0.5	Sidoli et al. (1999)
174417.2−293943	AX J1744.3-2940	266.07190	−29.66234	0.5	Sidoli et al. (2001)
174433.0−284427	Bursting pulsar	266.13788	−28.74096	0.5	Wijnands & Wang (2002)
174451.6−292042	KS 1741-293	266.21515	−29.34522	0.5	in't Zand et al. (1997)
174457.4−285021	*XMM* J174457-2850.3	266.23944	−28.83917	0.3	Sakano et al. (2005)
174502.3−285449	Granat 1741.9-2853	266.25983	−28.91397	0.4	Muno et al. (2003b)
174535.6−290133	AX J1745.6-2901	266.39853	−29.02612	0.4	Maeda et al. (1996)
174535.5−290124	...	266.39822	−29.02337	0.3	Muno et al. (2005)
174537.1−290104	1A 1742-289	266.40494	−29.01796	0.4	Davies et al. (1976)
174538.0−290022	...	266.40863	−29.00623	0.3	Muno et al. (2005)
174540.0−290005	...	266.41699	−29.00160	0.4	Muno et al. (2005)
174540.0−290030	...	266.41684	−29.00859	0.3	Muno et al. (2005)
174540.9−290014	...	266.42078	−29.00398	0.4	Muno et al. (2005)
174553.9−290346	*SWIFT* J174553.9-290347	266.47467	−29.06305	0.4	...
174554.4−285455	*XMM* J174554.4-285456	266.47690	−28.91533	0.4	Porquet et al. (2005)
174621.0−284342	1E 1743.1-2843	266.58768	−28.72868	0.4	Porquet et al. (2003)
174702.5−285259	SAX J1747.0-2853	266.76080	−28.88307	0.4	Wijnands et al. (2002)
...	*XTE* J1748-288	267.02108	−28.47383	0.6	Hjellming et al. (1998)
...	*XMM* J174544-2913.0	266.43546	−29.21683	4.0	Sakano et al. (2005)

of sources brighter than 2×10^{-6} photons cm^{-2} s^{-1} (2–8 keV) traces that of the old stellar population (Figure 12). This makes the population of X-ray sources in the Galactic center similar to those seen in globular clusters (e.g., Verbunt et al. 1997; Heinke et al. 2006).

Although the distribution of the majority of the X-ray sources traces that of the old stellar population, we have found 2.8σ evidence for an excess of sources in two regions where young, massive stars are forming: in the inner few arcminutes around Sgr A*, and in the region where the Arches and the Quintuplet star clusters lie. The excess of sources near these young star clusters also appears in the number of sources as a function of limiting flux, in which relatively more bright X-ray sources are found near the Arches and the Quintuplet (Figure 13 and Table 6). In total, these two regions contain a couple dozen more bright sources than our stellar mass model predicts. We suggest that these excess X-ray sources are part of the young stellar population in these regions (Mikles et al. 2006; Muno et al. 2006b; Mauerhan et al. 2007). In the near future, we will publish additional OB and Wolf–Rayet stars that have been identified through infrared spectroscopy of counterparts to X-ray sources (J. Mauerhan et al., in preparation).

A small fraction of the X-ray sources should be accreting black holes and neutron stars. Around 300 such X-ray binaries are known in the Galaxy, about half of which contain low-mass donors that overfill their Roche lobe, and half of which contain high-mass (OB and Wolf–Rayet) stars that donate mass through a stellar wind (Liu et al. 2006, 2007). These X-ray binaries are most easily identified when they are bright and variable (Muno et al. 2005). In total, over the history of X-ray astronomy, 19 X-ray sources in our survey field have been observed to be $> 10^{34}$ erg s^{-1} in X-rays, and have varied by at least an order of magnitude in X-ray flux (Table 7). Fifteen of these transient X-ray sources were bright during the time span of our *Chandra* observations (1A 1742-289 and *XTE* J1748-288 never entered outburst). Half of them have been discovered in the last nine years using *Chandra*, *XMM-Newton*, or *Swift* (e.g., Sakano et al. 2005; Porquet et al. 2005; Muno et al. 2005; Wijnands et al. 2006; Kennea et al. 2006). Surprisingly, despite having obtained 600 ks of new data in 2006 and 2007, we did not detect any new, bright ($> 10^{34}$ erg s^{-1}), transient X-ray sources. This suggests that we have identified all of the X-ray binaries that are active on timescales of a decade.

As mentioned in Section 2, the tables from this work will be available in the electronic edition of this journal, and additional products will be made available from the authors' Web site.[28] The data available from the authors' site includes FITS images of all of the images presented in this paper, as well as the averaged event lists, snapshot images, spectra, and calibration files for each source in the catalog. Combined with an increasing amount of multiwavelength data, this data set can be used to better understand the interactions between stars and interstellar media in the Galactic center, and the population of X-ray-emitting objects in general.

M.P.M., R.M.B., W.N.B., G.C.B., P.S.B., A.C., S.D.H., J.C.M., Q.D.W., Z.W., and F.Y.Z. received support from NASA through *Chandra* Award Number G06-7135 issued by the *Chandra* X-ray Observatory Center, which is operated by the Smithsonian Astrophsyical Observatory for and on behalf of the National Aeronautics Space Administration under contract NAS8-03060. T.J.W.L. and N.E.K. received funding for basic research in astronomy at the Naval Research Laboratory, which is supported by 6.1 base funding.

REFERENCES

Alexander, D. M., et al. 2003, AJ, 126, 539
Baganoff, F. K., et al. 2003, ApJ, 591, 891
Bauer, F. E., Alexander, D. M., Brandt, W. N., Schneider, D. P., Treister, E., Hornschmeier, A. E., & Garmire, G. P. 2004, AJ, 128, 2048
Buccheri, R., et al. 1983, A&A, 128, 245
Berghöfer, T. W., Schmitt, J. H. M. M., Danner, R., & Cassinelli, J. P. 1997, A&A, 322, 167
Brandt, W. N., et al. 2001, AJ, 122, 2810
Broos, P. S., Townsley, L. K., Getman, K., & Bauer, F. E. 2002, ACIS Extract, An ACIS Point Source Extraction Package (University Park: The Pennsylvania State Univ.), http://www.astro.psu.edu/xray/docs/TARA/.
Davies, R. D., Walsh, D., Browne, I. W. A., Edwards, M. R., & Noble, R. C. 1976, Nature, 261, 476

[28] http://www.srl.caltech.edu/gc_project/xray.html.

Ezuka, H., & Ishida, M. 1999, ApJS, 120, 277
Figer, D. F., Kim, S. S., Morris, M., Serabyn, E., Rich, R. M., & McLean, I. S. 1999, ApJ, 525, 750
Figer, D. F., Rich, M. R., Kim, S. S., Morris, M., & Serabyn, E. 2004, ApJ, 601, 319
Freeman, P. E., Kashyap, V., Rosner, R., & Lamb, D. Q. 2002, ApJS, 138, 185
Gaensler, B. M., & Slane, P. 2006, ARA&A, 44, 17
Gagné, M. , Oksala, M. E., Cohen, D. H., Tonnesen, S. K., ud-Doula, A., Owocki, S. P., Townsend, R. H., & McFarlane, J. J. 2005, ApJ, 628, 968
Getman, K. V., et al. 2005, ApJS, 160, 319
Heinke, C. O., Wijnands, R., Cohn, H. N., Lugger, P. M., Grindlay, J. E., Pooley, D., & Lewin, W. H. G. 2006, ApJ, 651, 1098
Hjellming, R. M., Rupen, M. P., & Mioduszewski, A. J. 1998, IAU Circ., 6934
Hogg, D. W. 2001, AJ, 121, 1207
Hong, J., van den Berg, M., Schlegel, E. M., Grindlay, J. E., Koenig, X., Laycock, S., & Zhao, P. 2005a, ApJ, 635, 907
in't Zand, J., Heise, J., Bazzano, A., Ubertini, P., Muller, J. M., & Smith, M. 1997, IAU Circ., 6618
Kennea, J. A., Wijnands, R., Burrows, D. N., Nousek, J., & Gehrels, N. 2006, Astron. Telegram, 920, 1
Kent, S. M., Dame, T. M., & Fazio, G. 1991, ApJ, 378, 131
Kilgard, R. E., et al. 2005, ApJS, 159, 214
Koyama, K., et al. 2007, PASJ, 59, S245
Kraft, R. P., Burrows, D. N., & Nousek, J. A. 1991, ApJ, 374, 344
Launhardt, R., Zylka, R., & Mezger, P. G. 2002, A&A, 384, 112
Law, C., & Yusef-Zadeh, F. 2004, ApJ, 611, 858
Laycock, S., Grindlay, J., van den Berg, M., Zhao, P., Hong, J., Koenig, X., Schlegel, E. M., & Persson, S. E. 2005, ApJ, 634, L53
Li, J., Kastner, J. H., Prigozhin, G. Y., Schulz, N. S., Feilgelson, E. D., & Getman, K. V. 2004, ApJ, 610, 1204
Liu, Q. Z., van Paradijs, J., & van den Heuvel, E. P. J. 2006, A&AS, 455, 1165
Liu, Q. Z., van Paradijs, J., & van den Heuvel, E. P. J. 2007, A&A, 469, 807
Lu, F. J., Wang, Q. D., & Lang, C. C. 2003, AJ, 126, 319
Lyons, L. 1991, A Practical Guide to Data Analysis for Physical Science Students (Cambridge: Cambridge Univ. Press)
Maeda, Y., Koyama, K., Sakano, M., Takeshima, T., & Yamauchi, S. 1996, PASJ, 48, 417
Marshall, D. J., Robin, A. C., Reylé, C., Schultheis, M., & Picaud, S. 2006, A&A, 453, 635
Mauerhan, J. C., Muno, M. P., & Morris, M. 2007, ApJ, 662, 574
Mauerhan, J. C., et al. 2009, ApJ, submitted
McNamara, D. H., Madsen, J. B., Barnes, J., & Ericksen, B. F. 2000, PASP, 112, 202
Mezger, P. G., & Pauls, T. 2002, in IAU Symp., 84, Proc. Symp., The Large-Scale Characteristics of the Galaxy (Dordrecht: Reidel), 357
Mikles, V. J., Eikenberry, S. S., Muno, M. P., Bandyopadhyay, R. M., & Shannon, P. 2006, ApJ, 651, 408
Muno, M. P., Baganoff, F. K., & Arabadjis, J. S. 2003b, ApJ, 598, 474
Muno, M. P., Baganoff, F. K., Bautz, M. W., Brandt, W. N., Garmire, G. P., & Ricker, G. R. 2003c, ApJ, 599, 465
Muno, M. P., Baganoff, F. K., Brandt, W. N., Morris, M. R., & Starck, J. L. 2007, ApJ, 669, 251
Muno, M. P., Bauer, F. E., Bandyopadhyay, R. M., & Wang, Q. D. 2006a, ApJS, 165, 173
Muno, M. P., Bower, G. C., Burgasser, A. J., Baganoff, F. K., Morris, M. R., & Brandt, W. N. 2006b, ApJ, 638, 183
Muno, M. P., Pfahl, E., Baganoff, F. K., Brandt, W. N., Ghez, A., Lu, J., & Morris, M. R. 2005, ApJ, 622, L113
Muno, M. P., et al. 2003a, ApJ, 589, 225
Muno, M. P., et al. 2004a, ApJ, 613, 326
Muno, M. P., et al. 2004b, ApJ, 613, 1179
Murdoch, H. S., Crawford, D. F., & Jauncey, D. 1973, ApJ, 183, 1
Perna, R., Narayan, R., Rybicki, G., Stella, L., & Treves, A. 2003, ApJ, 594, 936
Plucinsky, P. P., et al. 2008, ApJS, 174, 366
Porquet, D., Grosso, N., Bélanger, G., Goldwurm, A., Yusef-Zadeh, F., Warwick, R. S., & Predehl, P. 2005, A&A, 443, 571
Porquet, D., Rodriguez, J., Corbel, S., Goldoni, P., Warwick, R. S., Goldwurm, A., & Decourchelle, A. 2003, A&A, 406, 299
Preibisch, T., & Feigelson, E. D. 2005, ApJS, 160, 390
Psaltis, D. 2006, in Compact Stellar X-ray Source, ed. W. Lewin & M. van der Klis (Cambridge: Cambridge Univ. Press), 1
Ransom, S. M., Eikenberry, S. S., & Middleditch, J. 2002, AJ, 124, 1788
Reid, N. J. 1993, ARA&A, 31, 345
Revnivtsev, M., & Sazonov, S. 2007, A&A, 471, 159
Revnivtsev, M., Sazonov, S., Gilfanov, M., Churazov, E., & Sunyaev, R. 2006, A&A, 452, 169
Sakano, M., Warwick, R. S., Decourchelle, A., & Wang, Q. D. 2005, MNRAS, 357, 1211
Scargle, J. D. 1998, ApJ, 504, 405
Sidoli, L., Belloni, T., & Mereghetti, S. 2001, A&A, 368, 835
Sidoli, L., Mereghetti, S., Israel, G. L., Chiappetti, L., Treves, A., & Orlandini, M. 1999, ApJ, 525, 215
Skrutskie, M. F., et al. 2006, AJ, 131, 1163
Takagi, S., Murakami, H., & Koyama, K. 2002, ApJ, 573, 275
Townsley, L. K., Feigelson, E. D., Montmerle, T., Broos, P. S., Chu, Y.-H., & Garmire, G. P. 2003, ApJ, 593, 874
Trudolyubov, S., & Priedhorsky, W. 2004, ApJ, 616, 821
Verbunt, F., Bunk, W. H., Ritter, H., & Pfeffermann, E. 1997, A&A, 327, 602
Waldorn, W. L., & Cassinelli, J. P. 2007, ApJ, 668, 456
Walter, F. M., Wolk, S. J., & Neuhauser, R. 1996, Nature, 379, 233
Wang, Q. D. 2004, ApJ, 612, 159
Wang, Q. D., Dong, H., & Lang, C. 2006, MNRAS, 371, 38
Wang, Q. D., Gotthelf, E. V., & Lang, C. C. 2002a, Nature, 415, 148
Wang, Q. D., Lu, F. J., & Lang, C. C. 2002b, ApJ, 581, 1148
Warner, B. 1995, Cataclysmic Variable Stars (Cambridge: Cambridge Univ. Press)
Weisskopf, M. C., Brinkman, B., Canizares, C., Garmire, G., Murray, S., & van Speybroeck, L. P. 2002, PASP, 114, 1
Weisskopf, M. C., Wu, K., Trimble, V., O'Dell, S. L., Elsner, R. F., Zavlin, V. E., & Kouveliotou, C. 2007, ApJ, 657, 1026
Wijnands, R., Miller, J. M., & Wang, Q. D. 2002, ApJ, 579, 422
Wijnands, R., & Wang, Q. D. 2002, ApJ, 568, L93
Wijnands, R., et al. 2006, A&A, 449, 1117
Woods, P. M., & Thompson, C. 2006, in Compact Stellar X-ray Source, ed. W. Lewin & M. van der Klis (Cambridge: Cambridge Univ. Press), 547
Yusef-Zadeh, F., Law, C., Wardle, M., Wang, Q. D., Fruscione, A., Lang, C. C., & Cotera, A. 2002, ApJ, 570, 665